Numerical Study on Flexible Horizontal Axis Wind Turbine Rotors and Active Flow Control

アムル モハメッド アブドウエルハミッド モハメッド ハラワ

九州大学

Numerical Study on Flexible Horizontal Axis Wind Turbine Rotors and Active Flow Control

水平軸風車弾性ロータとアクティブフローコントロールに関する数値的研究

by

Amr Mohamed Abdelhamid Mohamed Halawa

アムル　モハメッド　アブドウエルハミッド
モハメッド　ハラワ

Submitted to the Earth System Science and Technology
in partial fulfillment of the requirements for the degree of

Doctor of Philosophy in Engineering

at

Kyushu University

September 2018

This page is intentionally left blank.

Numerical Study on Flexible Horizontal Axis Wind Turbine Rotors and Active Flow Control

by

Amr Mohamed Abdelhamid Mohamed Halawa

Submitted to the Earth System Science and Technology
on July 23, 2018, in partial fulfillment of the
requirements for the degree of
Doctor of Philosophy in Engineering

Abstract

The development of reliable Fluid-Structure Interaction (FSI) simulation tools and models for the wind turbines is a critical step in the design procedure towards achieving optimized large wind turbine structures. Such approach will mitigate the aeroelastic instabilities like: torsional flutter, stall flutter and edgewise instability that introduce extra stresses to the turbine structure leading to reduced life time and substantial failures.

The aim of this work was to study and achieve a better under-

standing of the aerodynamics of wind turbine blades and their related challenges, using various CFD simulations. Several issues were addressed, mainly the fluid-structure interaction (aeroelastic) effects on the wind turbine blades as well as the stall phenomenon with promising solutions to it using active flow control. The computations results were quite satisfactory and could represent a good foundation for future work in this area.

In this study, CFD simulations were carried out in order to calculate the stall characteristics and choose a suitable turbulence model for the DU96-W180 airfoil, developed by Delft University of Technology (TUDelft) and dedicated to wind turbines. The results were validated with the experimental wind tunnel results of TUDelft. The computations were carried out till the complete unsteady Kármán vortex shedding is formed in the airfoil's downstream wake. The results showed a successful capture of the stall phenomenon with an acceptable error margin. OpenFOAM®'s *pisoFOAM* solver alongside k–ω SST turbulence model showed reliability in matching the physics of the problem.

In addition, FSI simulations were held to the full-scale rotor blades of the NREL 5MW reference horizontal axis wind turbine. They were implemented using the vortex-based, MIRAS-FLEX of the Technical University of Denmark (DTU), as well as the CFD-based Ansys FLUENT. The aerodynamic loads and structural responses computations were carried out using a steady-state FSI analysis. Finally, the results were compared and validated against another widely used BEM-based aeroelastic codes as FLEX5-Q^3UIC and FAST codes in different cases showing reasonable agreement.

Furthermore, in order to solve some associated stall-problems near the blade tips, a novel active flow control technique was tested on a wind turbine airfoil to investigate on the improvement of its aerodynamic performance. Numerical simulations were done for incompressible unsteady low Reynolds Number flow at high angle of attack. The flow control was achieved using an "Active Slat" where the periodic blowing effect was achieved by periodically opening and closing the slat passage. The merit of this concept is being flexible and activated only based on the requirements from a desired operating condition. A new OpenFOAM® solver was developed

from the existing pisoFoam solver to simulate the active slat flow control technique. Various approaches were used to achieve the optimum excitation frequency for the active slat operation so that the best aerodynamic performance is guaranteed. Finally, good improvements were achieved in the lift coefficient and aerodynamic efficiency. Hence, that dictates a promising application on any blade surface experiencing stall issues or separated flows at higher angle of attack.

Thesis Supervisor: Dr. Shigeo Yoshida
Title: Professor
Date: 23/07/2018

Acknowledgments

Firstly, I would like to express my sincere gratitude and thanks to my supervisor Prof. Shigeo Yoshida for his unprecedented scientific guidance, constructive supervision, valuable instructions and generous support. I have learned a lot and widened my knowledge from our constructive discussions and your great experience. Thanks for your patience and support in overcoming numerous obstacles I have been facing through my research. You were really a role model for the devotion and dedication to work and achieve astonishing results. Honestly, I could not have imagined having a better advisor and mentor for my PhD study.

In addition, I would like to thank Prof. Changhong Hu and Assoc. Prof. Takanori Uchida for their time and efforts spent for the review of this work. Their respectful comments and suggestions are really appreciated and improved the quality of the work.

Thanks to the Ministry of Education, Culture, Sports, Science, and Technology (MEXT), Japan Government, for funding my funded my PhD studies. Additionally, thanks to the Interdisciplinary Graduate School of Engineering Sciences (IGSES), Kyushu University, funding my conferences, workshops and internships. Their support is much appreciated.

Moreover, I would like to thank all the community of Kyushu University for encouraging me to do my best and learn as much as I can every day. I would also like to thank all the staff of the Earth System Science and Technology (ESST) Department who never hesitated to support and assist me whenever I needed. Thanks to Dr. Makoto Sueyoshi and Dr. Yingyi Liu for their support and fruitful discussions. Thanks a lot to Ms. Sakura Kawasaki for her tremendous support and

professional work. Thanks also to Ms. Masako Yoshizu, Ms. Yukiko Matsuse, and Mr. Masahiro Hamasaki.

A major portion of this work would not have been done without the valuable guidance and discussions with the Technical University of Denmark professors and staff. Special thanks to Prof. Wen Shen and Dr. Matias Sessarego. I had really learned a lot from our discussions and your valuable comments on my work. Thanks also to Prof. Sørensen, Dr. Néstor, and Dr. Hamid for our fruitful discussions. Special thanks goes to Helle and Lone for your kindness and care that made my life easy and smooth in Denmark. I really appreciate all your support. Thanks to my friends Ayman, Lorenzo, Kaya, Alsah, Emre, Antonio, Bruno, Dominic and Friis for the fun time we spent together and the memories that will stay with me for a lifetime.

Special thanks to my first Japanese friends Mitarai, Yoshimizu and Ni for your kind support and guidance in my first period in Japan. Your help had made my life much easier and is really much appreciated. Thanks to Ms. Kojima for her everlasting support, kindness to help us whenever we face any problems, and organizing wonderful events that were full of fun. Thanks also to Ms. Fukushima and Ms. Akashi for their kind support. Thanks also to my dear friends at KIISA and KUFSA for the wonderful time we spent together.

Nevertheless, I am also grateful to all my professors in Cairo University for laying the strong foundation of my scientific background. Their kind help, guidance and support are much appreciated.

Furthermore, I would like to thank my dear friends Amr Metwally, Tarek Dief,

Rushdi, Kamra, Omar for your continuous support and bearing up with me and encouraging in my tough moments. I am really so grateful to you. Thanks also to my dear friend Dr. Uli Göltenbott for his constructive discussions besides his nice sense of humor and fun moments that really relieves me out of the work stress. Thanks also to Dr. Ahmed El-Sayed for his kind advice and support. Many thanks goes to my dear friends Moadh, Irina, Bai, and Bryan for the awesome time and events we had together. I will never forget our gatherings with you all; you are wonderful guys and true friends. My life in Japan was made enjoyable mainly thanks to you. Additionally, I would like to thank my friends Tarek, Hatem, Sameh, Nasef, Ibrahim, Islam, Ali, Egiza, Lotfy, and all my fellow labmates for their continuous encouragement and fun time we had together. Thanks also to Ameer and Karim for your kind best wishes for me.

Last but not least, I would like to express my deepest feelings and profound gratitude to my dear parents; Dr. Mohamed, Mrs. Amal, brother; Ali, sisters; Noha, Nihal, and Hasnaa for their surpassing sacrifices, deep belief in me and non-stop encouragement. Actually, without them, I would never be able to pursue this work. Thank you for your patience throughout all the years. I am forever grateful. Thanks to all my family for their faithful wishes, continuous care and support. I love you all and hope to achieve your ambitions.

Amr Halawa

Kyushu University

July, 2018

This page is intentionally left blank.

Declaration

No portion of the work referred to in the thesis has been submitted in support of an application for another degree or qualification of this or any other university or other institute of learning.

This page is intentionally left blank.

Nomenclature

Acronyms

2D	Two Dimensional flow
3D	Three Dimensional flow
ABL	Atmospheric Boundary Layer
ADM	Actuator Disk Model
AFC	Active Flow Control
ALE-VMS	Arbitrary Lagrangian–Eulerian Variational Multi-Scale
ALM	Actuator Line Model
BEM	Blade Element Momentum
CFD	Computational Fluid Dynamics
DNS	Direct Numerical Simulation
DOFs	Degrees Of Freedom
DTU	Technical University of Denmark
DU	Delft University airfoil series
FAST	Fatigue, Aerodynamics, Structures, and Turbulence Code of NREL
FFT	Fast Fourier Transform
FSI	Fluid-Structure Interaction
HAWC2	Horizontal Axis Wind turbine simulation Code 2nd generation
HAWT	Horizontal Axis Wind Turbine

HPC	High Performance Computing
IDDES	Improved Delayed Detached Eddy Simulation
KU	Kyushu University
LES	Large Eddy Simulation
MEMS	Micro-Electro-Mechanical-Systems
MEXICO	Model EXperiments In COntrolled conditions
MIRAS	Method for Interactive Rotor Aerodynamic Simulations
MLSM	Modified Linear Stochastic Measurement
MPI	Message Passing Interface
NREL	National Renewable Energy Laboratory
NS	Navier–Stokes equations
OpenFOAM	Open source Field Operation And Manipulation
PFC	Passive Flow Control
PISO	Pressure implicit with splitting of operator
POD	Proper Orthogonal Decomposition
Q^3UIC	Quasi-3-dimensional Unsteady viscous-inviscid Interaction Code
RANS	Reynolds-Averaged-Navier-Stokes equations
ROM	Reduced-Order Model
SGS	Sub-Grid-Scale
SST	Shear Stress Transport turbulence model by Menter
TSR	Tip Speed Ratio
TUDelft	Delft University of Technology
VG	Vortex Generators
ZNMF	Zero-Net Mass-Flux

Greek Symbols

α	Angle of attack

Δ	Difference / Change operator
ϵ	Turbulent dissipation rate
$\overline{\nabla}$	Non-dimensional gradient parameter
μ	Dynamic viscosity
μ_{air}	Dynamic viscosity of air
∇	Gradient operator vector, its 2D Cartesian coordinates: $[\frac{\partial}{\partial x}, \frac{\partial}{\partial y}]^T$
ν	Kinematic viscosity
ν_{air}	Kinematic viscosity of air
ν_{SGS}	Subgrid-scale viscosity
ω	Dissipation rate of the turbulent kinetic energy
ρ	Density
ρ_{air}	Density of air

Roman Symbols

$\bar{U}_y$	Normalized cross-stream velocity
$\boldsymbol{u}$	Velocity (vector) variable
$\overline{u'u'}$	Reynolds stress tensor
$\overline{u}$	Average velocity component
$\tilde{u}$	Resolvable scale part of velocity
$\widetilde{G}_k$	Generation of turbulence kinetic energy due to velocity gradients
A	Area of the disc
a	Induction factor
c	Chord length
C_D	Drag coefficient
C_L	Lift coefficient
C_L/C_D	Aerodynamic efficiency
C_P	Power coefficient

C_p	Pressure coefficient
C_T	Thrust coefficient
D_ω	Cross-diffusion term in the k–ω turbulence model
$\bar{f}$	Non-dimensional frequency parameter
G_ω	Generation of the dissipation rate of the turbulent kinetic energy
k	Turbulent energy
L	Characteristic length scale (e.g. the chord length for airfoil sections)
M	Mach number
P	Power extracted
p	Pressure (Scalar) variable
$\overline{p}$	Non-dimensional pressure, Average pressure
Re	Reynolds number
S_ω	User-defined source term in the k–ω turbulence model
S_k	User-defined source term in the k–ω turbulence model
T	Aerodynamic thrust
t	Time variable
$\bar{t}$	Non-dimensional time
U	Velocity (vector) variable
$\overline{U}$	Non-dimensional velocity
u'	Fluctuating velocity component
u''	Subgrid-scale part of velocity
U_∞	Free stream velocity
U_d	Velocity at the disc
U_y	Cross-stream velocity
Y_ω	Dissipation of ω due to turbulence
Y_k	Dissipation of k due to turbulence

Other Symbols

$\cdot$	Scalar (Dot) product operator
i, j	Generic indices
®	Registered trademark
^{o}	Measure of an angle in degrees
^{T}	Transpose operator

This page is intentionally left blank.

Contents

This page is intentionally left blank.

List of Figures

This page is intentionally left blank.

List of Tables

This page is intentionally left blank.

Chapter 1

Introduction

Contents

1.1 Nature of Wind Energy

Wind is a free, clean, and readily available renewable source of energy. It is a different form of solar energy caused by many reasons like the uneven atmospheric

heating by the sun, the earth's rotation, and surface irregularities. The Earth's surface varies in its shape and consistency. It has mountains, lakes, deserts, plains, forests, and oceans. Each of those absorbs the sunlight in a different extent, causing that uneven local heating on the earth's surface. The hot air will expand and rise upwards in the warmer areas, causing a drop in the air pressure [1]. Thus, the neighboring higher pressure air flows to the low-pressure region to replace that rising hot air as shown in Figure 1-1.

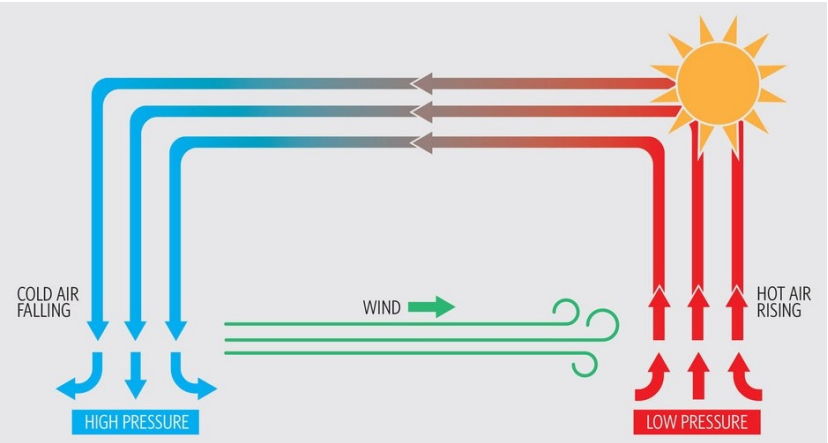

Figure 1-1: Wind flow mechanism [1].

These wind flows carry enormous amount of energy that needs to be harvested. To achieve this, the kinetic energy is needed to be converted into mechanical energy then electrical energy. Such energy flow is captured each day, around the world, by modern wind turbines and converted into electricity. Obviously, faster flowing winds possess more energy content. Similarly, wind turbines with a larger surface area will capture more wind and should produce more power. This source of power generation plays an increasingly important role in the way we power our world [2, 3].

1.2 Brief History on Wind Power

Harnessing wind energy dates back to the earliest recorded history. Wind energy was used by the Ancient Egyptians to propel their sailing boats along the Nile river as far as 5000 years ago in the Pharaonic Egypt as shown in Figure 1-2.

Figure 1-2: Wind-powered Pharaonic boat sailing along the Nile River [7].

As early as 200 years B.C, the first documented use of wind on land was made in ancient Babylon. Besides, simple windmills were used by the Chinese to pump water at this time. In addition, in the Middle East and Persia, woven reed sails on vertical-axis windmills were used to grind grains [4]. By the year 250 A.D., the Roman Empire got to use the wind turbines. Later by the 7th century, the first practical windmills were used in Sistan, Afghanistan [5, 6].

New ways of using the energy of the wind eventually spread around the world. By the 11th century, people in the Middle East used windmills extensively for food production. Returning merchants and crusaders carried this idea back to Europe.

The Dutch refined the windmill and adapted it for draining lakes and marshes in the Rhine River Delta as shown in Figure 1-3. When settlers took this technology to the New World in the late 19th century, they began using windmills to pump water for farms and ranches and later to generate electricity for homes and industry.

Figure 1-3: An old Dutch windmill [8].

Americans used windmills to grind wheat and corn, to pump water and to cut wood at sawmills. With the development of electric power, wind power found new applications in lighting buildings remotely from centrally generated power. Throughout the 20th century, small wind plants, suitable for farms and residences, and larger utility-scale wind farms that could be connected to electricity grids were developed. During World War II, the largest wind turbine known in the 1940s, a 1.25-megawatt turbine that sat on a Vermont hilltop known as Grandpa's Knob, fed electric power to the local utility network. Wind electric turbines persisted

in Denmark into the 1950s but were ultimately sidelined due to the availability of cheap oil and low energy prices. The oil shortages of the 1970s changed the energy picture for the U.S. and the world. It created an interest in alternative energy sources, paving the way for the re-entry of the wind turbine to generate electricity [4, 9].

Nowadays, the trend of wind turbines' size is getting larger which is necessary to improve the cost of wind energy and make it more efficient and feasible as shown in Figure 1-4. The largest wind turbine in operation at this point in time is the Vestas V164 [10] with 8MW capacity, rotor diameter 164m with a weight of each blade between 33 and 35 tons. Currently, researchers in DTU focus on developing technologies to upscale single-rotor wind turbines beyond 10 MW [11].

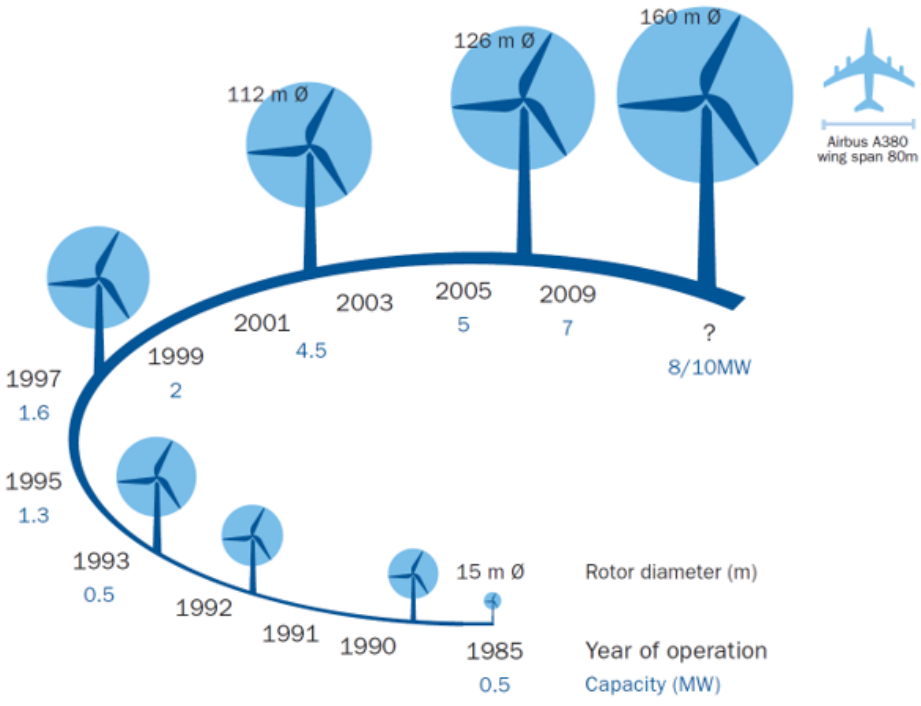

Figure 1-4: Size evolution of wind turbines over time [12].

Wind turbines have without any doubt been very important for the evolution of modern society. The turbine will also be very important in the future when energy systems world wide must be replaced by renewable energy systems [6, 14].

1.3 Outlook on the Global Wind Energy

Wind energy is plentiful, readily available, and capturing its power does not deplete our valuable natural resources. In fact, wind turbines can help to counter the detrimental effects of climate change. The Global Wind Energy Outlook projects that by 2030 wind energy will offset 2.5 billion tons per year of carbon dioxide. This is equivalent to taking 530 million cars off the road each year or avoiding the use of 4.6 billion barrels of oil globally. This would even offset emissions from 525 coal-fired power plants in one year. [2]

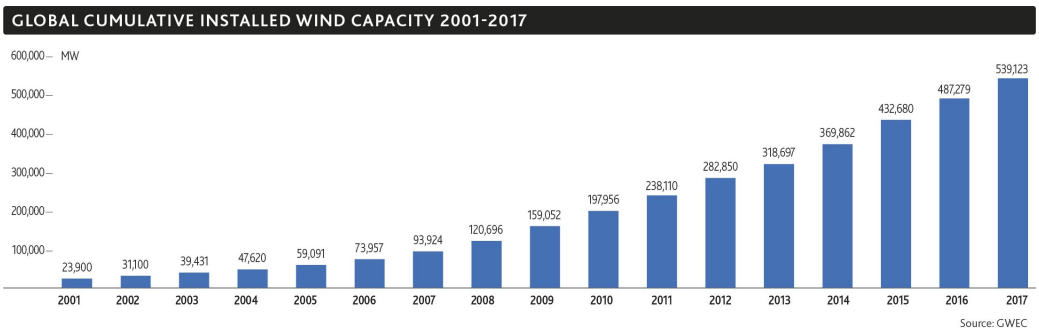

Figure 1-5: Global cumulative installed wind capacity 2001-2017 [15].

In the recent years, the wind energy utilization for electricity production has been increasing. The global installed wind power capacity had reached around 540 GW as of 2017 as shown in Figure 1-5 according to the half year report by the Global Wind Energy Council (GWEC) [15]. The report also shows how the global installed capacity of wind power has increased in the last years in different

regions around the world as shown in Figure1-6.

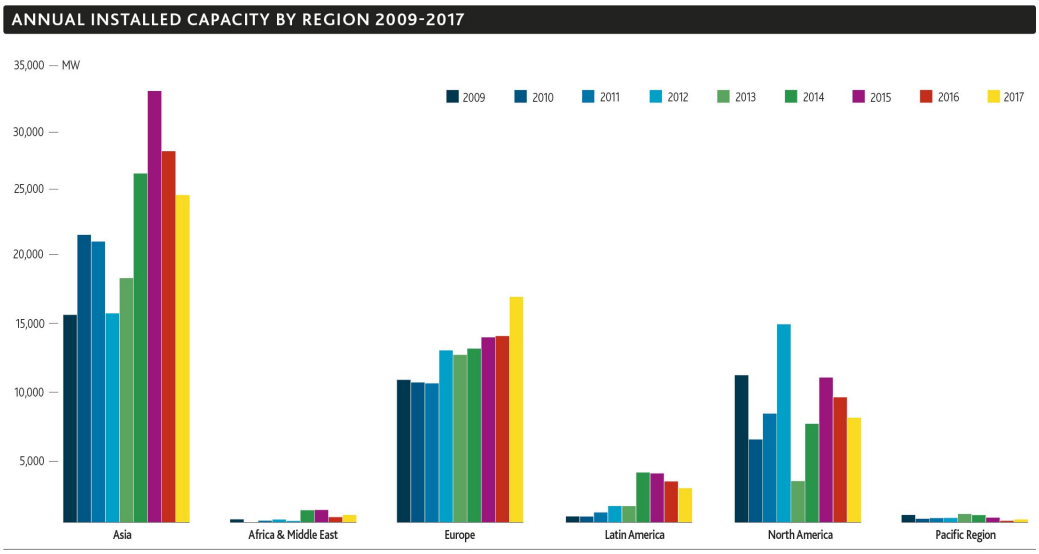

	2009	2010	2011	2012	2013	2014	2015	2016	2017
Asia	15,507	21,481	20,981	15,624	18,252	26,058	33,962	27,721	24,412
Africa & Middle East	251	153	8	131	240	934	953	418	618
Europe	10,660	10,466	10,393	12,862	12,524	12,988	13,831	13,926	16,803
Latin America	471	459	771	1,248	1,240	3,744	3,678	3,078	2,578
North America	11,008	6,208	8,137	14,807	3,112	7,382	10,829	9,359	7,836
Pacific Region	578	294	345	358	655	568	381	140	245

Source: GWEC

Figure 1-6: Annual installed wind capacity by region 2009-2017 [15].

As of 2015, 42.1% of Denmark's energy supply comes from wind power. (Top of the world). The biggest wind turbine manufacturers with production facilities in Denmark are Vestas and Siemens Wind Power. Vestas, as the biggest name in the wind industry, owns a market share of 12.3% with more than 60 GW installed worldwide [13].

1.4 Capabilities of CFD Application in Wind Energy

With Computational Fluid Dynamics we indicate the numerical solution of the differential governing equations of fluid flows, with the help of computers. This

technique has a wide range of engineering applications. In the field of aerodynamic research this technique has become increasingly important and it is prominent for studying turbo-machinery [16].

A number of valuable advantages are achieved following a CFD approach to a fluid dynamic problem:

- CFD is faster and definitely cheaper. A considerable reduction of time and costs for solving the problems is offered compared to the traditional approaches. A conscious assessment of different solutions is available in the early phase of the design process, in order to fit with the requested tasks. Thus, experimental tests would be done just on few models, resulted from the CFD analysis.
- Full-size analysis is hard to perform for large systems, like modern wind turbines are, or for extreme thermo-flow conditions as well as narrow geometries. A CFD study is a favorable choice in these cases.
- A key–important quality of CFD are the detailed solutions allowed by the recent techniques (and computer technologies), even for time-dependent flows and complex systems.
- The numerical models of the physical problems have good accuracy and reliability, due again to the newest mathematical improvements of solution schemes and of turbulence models.
- Due to the last two advances, in most of the cases the prediction of a fluid dynamic problem does not require a dedicated powerful workstation and sometimes a personal computer might be sufficient.

The numerical modeling of a fluid dynamics problem implicates first a precise reading of the physical phenomena. All the relevant features of interest should be indicated at that first step, including geometry, materials, boundary conditions, to be defined in the simplest way, but without introducing extreme errors with the hypothesis. Nevertheless, a number of simplifications is always accepted, and is inevitable in order to model properly fluid dynamics problems [16].

1.5 Challenges in Wind Turbine Aerodynamics

1.5.1 Aerodynamic Separation

Wind turbines are usually vulnerable to aerodynamic stall when their blades are struck by a relative wind at high angle of attack. This phenomenon occurs in storm conditions with large yaw misalignment and also in power production in turbulent wind. This will result in stall-induced vibrations which deteriorate the aerodynamic performance of the blade as well as imposing extra stresses on the blade structure through fatigue loads, and might potentially end up to wind turbine failures. Thus, accurate prediction of the stall and post-stall characteristics of the wind turbine blades is an important preliminary step towards a full understanding of the flow behavior in this critical region to reduce the design loads, hence, to reduce the cost. Consequently, this will facilitate the process of choosing the optimum control technique for delaying the separation or even reattaching it back to the surface of the wind turbine blade. Hence, the stall-related undesirable consequences could be much mitigated or even hindered and that will surely have a noteworthy practical impact on improving wind turbine power outcome at a reasonable energy cost.

1.5.2 Fluid-Structure Interaction

The increased potential for the extraction of wind energy has led to a considerable development in the wind turbines designs. The turbine blades are getting larger and thus introducing new load effects. The flexibility of large wind turbines yields an interaction between the fluid flow and the internal structure loading causing what is known as Fluid-Structure Interaction (FSI) or aeroelastic effects. The consequences of these effects are many instability problems like torsional flutter, stall flutter and edgewise instability imposing extra stresses on the blade structure through fatigue loads that potentially end up to wind turbine failures. Hence, developing reliable FSI simulation tools and models for the blades of wind turbines is a critical step towards developing and optimizing the large wind turbines designs. Many recent studies are centered around the FSI development. Hsu and Bazilevs [17] simulated a full scale turbine using a fully coupled 3D FSI approach by a low order FEM-based ALE-VMS technique. Rafiee et al. [18] investigated the aeroelastic behavior using modified BEM and CFD then constructed an iterative FSI approach. Wang et al. [19] established an FSI model using CFD and FEA with one-way coupling interface between them. Carrión et al. [20] applied a CFD-CSD method to perform aeroelastic analysis on NREL and MEXICO wind turbines where flapwise and edgewise instabilities were studied. Recently, Heinz et al. [21] conducted a high-fedility study on the blade of the reference wind turbine DTU 10 MW to investigate the aeroelastic response in deep stall conditions using HAWC2CFD tool [22]. Dose et al. [23] coupled OpenFOAM to an in-house structural beam solver to investigate the aeroelasticity of the NREL 5MW wind turbine blade at high wind speeds.

In the current work, FSI simulations were held using both vortex-based and CFD-based methods. An incompressible coupled pressure-based solver was used

in Ansys Fluent to compute the aerodynamic loading on the rotor blades. Then, the pressure loads were passed on to Ansys Mechanical to calculate the induced stresses and deformations of the blade. This solver was applied to the full-scale rotor blades of the NREL 5MW reference horizontal axis wind turbine (HAWT) [24] shown in Figure 1-7. Furthermore, a dynamic mesh was used to consider the deformations and displacements in the FSI interface. The computations were run on the Kyushu University multi-core Linux cluster server using the public domain openMPI implementation of the standard message passing interface (MPI). Afterwards, the solver results were validated against the Technical University of Denmark's (DTU) MIRAS-FLEX [25] aeroelastic code results as well as the widely used BEM-based FLEX5-Q^{3}UIC [26] and FAST [27] codes in different cases.

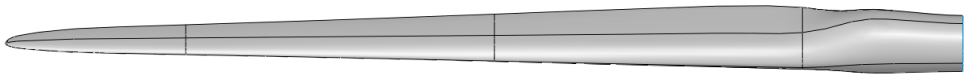

Figure 1-7: The NREL 5 MW wind turbine blade [24].

1.5.3 Flow Control

Flow control studies and its relevant applications had experienced great development in the past few decades. It is a fast growing multi-disciplinary scientific field aiming at changing a natural state of flow to a more efficient state. Modern flow control methods are majorly applied to achieve drag reduction, lift enhancement, transition delay, separation postponement, mixing augmentation, flow-induced noise suppression, turbulence management ... etc [28–31]. Controlling the complex flow structures and achieving a mature understanding of their behavior and characteristics will surely have a noteworthy practical impact. The shapes

and dimensions of any wings, blades, nozzles, diffusers, combustion chambers, ground/submerged vehicles, and so forth will be highly renovated. Moreover, new efficient designs could be achieved that allow for applications at higher speeds, range, and endurance yet with less fuel consumption. Furthermore, in case of wind turbine blades, the power production will be much maximized. Simply, any mechanical machinery related to the flow of fluids, whether externally or internally, will probably have a different looking and performance in the forthcoming decades [29–31].

Flow control techniques can be categorized as follows according to:

- Actuation type: Passive (steady) / Active (unsteady).
- Response of the actuation system to the flow changes: Open-loop (feedforward) control / Closed-loop (feedback) control.

1.5.3.1 Passive Flow Control

Passive flow control (PFC) is considered by its nature an open-loop system since it couldn't respond to the flow changes. It includes vortex generators, riblets, spoilers, strakes, steady blowing or suction, and others. From the benefits of PFC is that it's simple, light, less expensive in its design and manufacturing phase, and can be easily maintained compared to active flow control; therefore PFC is more susceptible to be implemented in many applications in the real-word. On the other hand, PFC has disadvantages one of which is that it might posses limited range of effectiveness during the flight conditions while on the rest of the flight it deteriorates the overall flight performance.

One example of PFC is the Vortex Generators (VG) developed by many com-

panies like Boundary Layer Reserach, and Micro Aerodynamics Inc., and others that was successfully implemented in many practical applications. As shown in Figure 1-8, VG are located at a spanwise-line nearly 10% after the wing leading edge. They energize the wing upper surface stagnant boundary layer by controlling the flow of the air through creating vortices. Thus, the flow will stick better to the wing improving the aircraft performance allowing a controlled flight at higher angle of attacks and lower airspeeds.

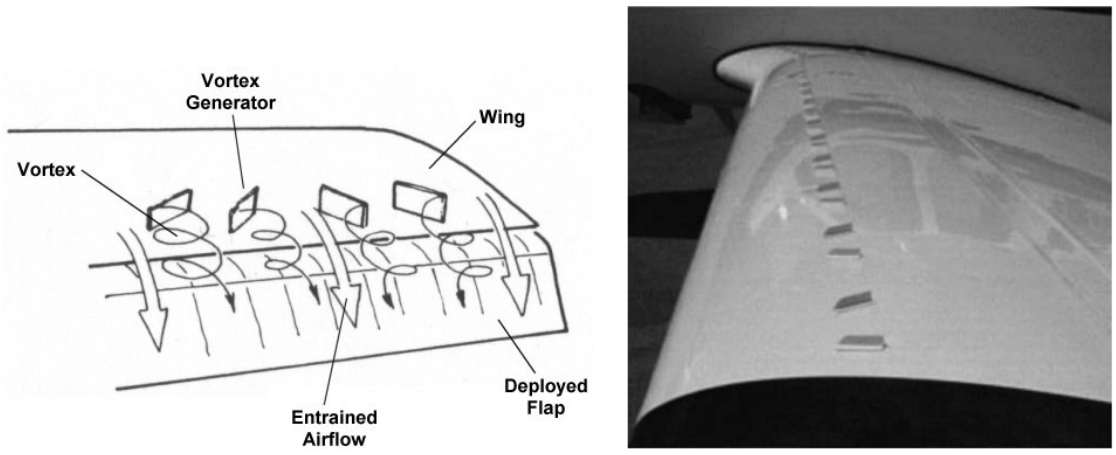

(a) (b)

Figure 1-8: (a) VG schematic vortices on wing. (b) VG practical implementation on Beech Bonanza wing [34].

Besides, studies by Jirásek [32] in 2005 shows promising results using new VG model characterized by simplicity in implementation and high ability to reproduce results using computational fluid dynamics (CFD). More recently, PFC was successully applied in cavity flows by Yamouni [33] in 2013.

1.5.3.2 Active Flow Control

Active flow control (AFC) can generally be classified as the control strategy that needs to input energy to change the dynamics of the flow or the steady-state of

the flow so that the average of the mean flow with respect to time is changed. Actuation can be steady or periodic fluid addition though suction or blowing from surface slots. It also implies momentum injection by periodic motion of actuators like flaps or thin membranes. AFC is more flexible and shows better performance compared to PFC. It can be adapted to any specific flight condition. Besides, when not essential (as the case of off-design conditions), it can be shut down. Moreover, it yields lower drag than fixed PFC devices that drags the fluid flow all the time. On the other side, it implies injecting actuation energy to the flow so the benefit to cost ratio should be calculated precisely for better feasibility. Its implementation is somehow complicated and thus needs special physics scaling to be applied in real-life.

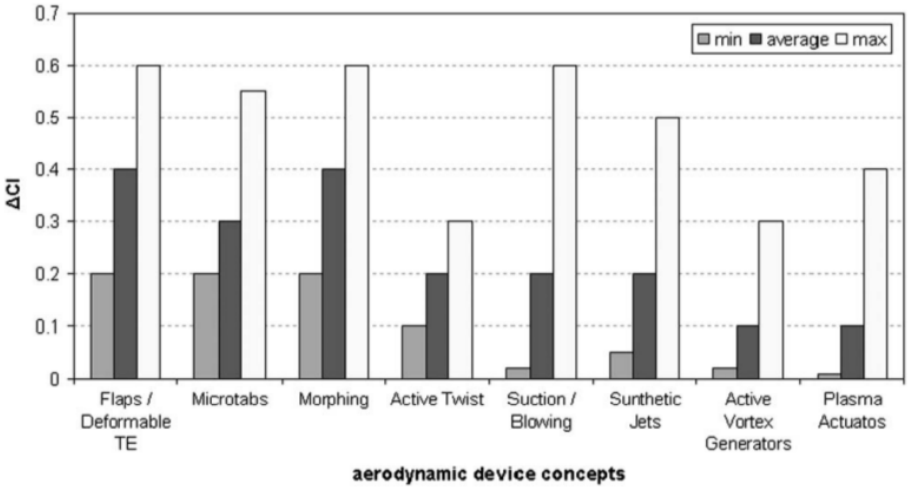

Figure 1-9: Comparison among different actuators for achieved lift enhancement [35].

There are so many successfully applied flow control applications starting from Passive Flow Control (PFC) actuators to the modern Micro-Electro-Mechanical-Systems (MEMS). A good quantitative comparison was performed by Barlas and Kuik [35], as shown in Figure 1-9, for the improved aerodynamic performance

of wind turbines flow using different actuators. The feasibility of these active flow control AFC actuators was discussed where Microtabs showed high lift performance in addition to their simplicity and low power consumption. Morphing (camber control) method was highly efficient for increasing lift but difficult from the perspective of structure implementation until new techniques and smart materials could be used. One of the promising flow control actuators was the trailing edge flap that showed high lift improvement while being simple with linear response. It was applied successfully in free shear flows by Cattafesta et al.[36] in 2001 as well as its application in flow-induced cavity oscillations by Mathew et al. [37] in 2006.

On the other hand, Active Twist showed remarkable flow control yet it was not efficient technique. It suffered heavy blades, high power consumption and elevated operational cost. The remaining boundary-layer-based flow control techniques (synthetic jets, suction/blowing, plasma, etc) showed enhanced lift for high angles of attack near stall, however insignificant effect at low angles of attack [38]. Furthermore, Zero-net mass-flux (ZNMF) actuators, frequently called synthetic jets, were successfully implemented in many applications in the flow control field as noted by Glezer and Amitay [39] in 2002 and also by Raju et al. [40] in 2005. The popularity of ZNMF actuators in many applications is because they do not need any external source of flow, aside from their ability to produce complex vortices using different transduction schemes. Recently, plasma actuators have acquired great reputation among researchers since they have rapid time response due to the absence of moving parts, along with their solid-state nature, and small weight [41]. It has been studied extensively by Moreau [42] in 2007 and Corke et al. [43] in 2010.

Moreover, slats are aerodynamic surfaces attached to the wing leading edge

allowing the passage of the air from below its lower surface to the upper surface. They provide some kind of blowing control into the boundary layer by a fresh jet of air that has higher energy than that of the boundary layer as shown in Figure 1-10. That fresh jet of air adds an extra flow momentum to the upper surface flow that enhances the mixing of flow in the boundary layer. Consequently, a thicker boundary layer profile is achieved that can withstand high adverse pressure gradients and maintain attached flow (delaying separation) for longer distances. As a result, improved aerodynamic efficiency and operation at reduced stall speeds and higher angles of attack could be easily achieved. It also reduces the high concentrated pressure near the leading edge by changing the camber of the nose [44, 45].

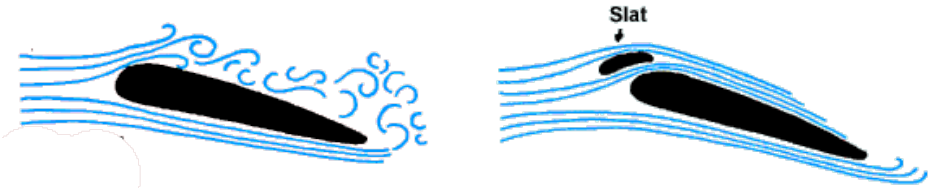

(a) (b)

Figure 1-10: Flow over: (a) Clean airfoil. (b) Slatted airfoil.

Based on the study of Elhadidi et al. [46], an active slat on DU96-W-180 airfoil was implemented as in Figure 1-11a where the blowing effect was achieved by the means of a simply designed actuator which is a vane rotating inside a stationary slat. The main benefit is its flexibility according to the specified operating condition. It might be fully closed, open or even actuated actively to induce the flow. Their experimental results indicated success in achieving a reduced mean pressure and an increased mean velocity on the upper surface of the airfoil at all the studied positive angles of attack, thus higher resultant lift as in Figure 1-11b.

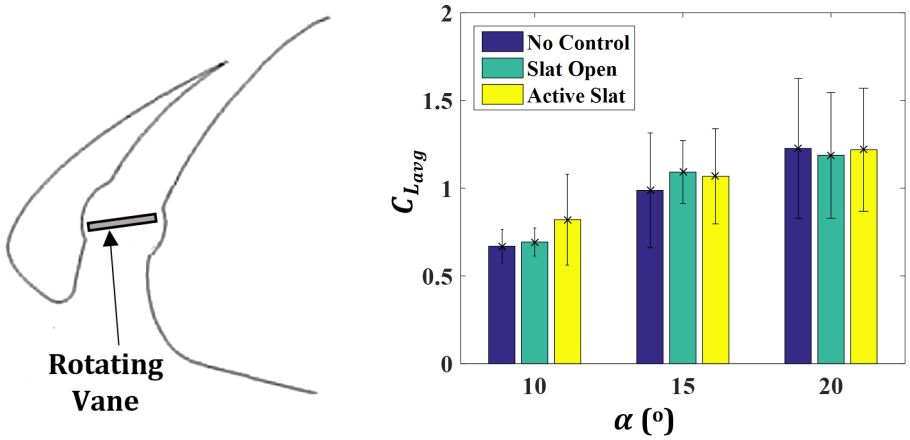

(a) (b)

Figure 1-11: The active slat study: (a) Active slat actuator modeling. (b) Comparison between the lift coefficient numerical results for different cases [46].

1.6 Motivation and Objective

Wind energy is a low density source of power. To make wind power economically feasible, it is important to maximize the efficiency of converting wind energy into mechanical energy. Among the different aspects involved, rotor aerodynamics is a key determinant for achieving this goal. In addition, the ability to predict the downstream wake from a wind turbine is a significant factor for determining the interactions between turbines. Research work conducted in this area has brought to a substantial improvement in the overall efficiency of the conversion process, with the result that the capital costs of installing wind power can now compete effectively with other energy sources. Three approaches are available to analyze the flow around and downstream of a wind turbine: field or wind tunnel testing, which provides accurate results but is highly complex and expensive; analytical and semi-empirical models, which adopt simplifying assumptions and are thus

not universally reliable; and CFD, which probably offers the best support or alternative to direct measurements [47].

The aim of this PhD project was to realize a comprehensive study of HAWT aerodynamics, by numerically solving the fluid dynamic problem with the help of a finite-volume Navier–Stokes (NS) CFD solvers and showing the interaction effect with the structural part. Besides, introducing some promising solution to the stall problem on the wind turbine blades.

1.7 Thesis Overview

This thesis consists of 5 main chapters. Chapter 1 gives a short introduction on where wind energy stands today along with potential and challenges. Besides, it shows a brief history on wind power, the nature of wind energy, and an outlook on the global wind power utilization. Moreover, the capabilities of CFD applications in wind energy as well as the objective and motivation are included.

In Chapter 2, some basic background theory on the aerodynamics of wind turbines is presented. Besides, more focus on the wind turbine Computational Fluid Dynamics is shown alongside the turbulence modeling and the discretization technique used in this work.

Chapter 3 shows the Fluid-Structure Interaction study where it starts with a pre-computational study on the wind turbine airfoil DU96-W-180. That study yielded some important parameters to consider in the following simulations like the turbulence model and the appropriate mesh sizing to capture the physical be-

havior of the flow at near-stall angles of attack. Next, a vortex-based method for FSI simulations is discussed showing some sample results on the NREL 5MW HAWT rotor. Afterwards, CFD-based method is introduced for FSI simulations showing various aerodynamic and structural properties of the NREL 5MW HAWT rotor. Finally, for the sake of validation, a comparison between various codes were carried out showing a good agreement and useful suggestions for future extension of this work.

In Chapter 4, the Active Flow Control flow control approach is presented with the active slat technique. Open-loop simulations using different excitation frequencies are investigated to show the impact on aerodynamic properties. Furthermore, the numerical analysis of the base case including frequency analysis technique as well as the slatted airfoil results are shown. Finally, the results were recorded and compared showing promising application of this technique for future similar applications.

Last but not the least, Chapter 5 summarizes the thesis main conclusions besides showing some recommendations for future work.

This page is intentionally left blank.

Chapter 2

Theoretical Background

Contents

2.1 Introduction

With the shortage of fossil fuels and the increase of environmental awareness, renewable energy is becoming more important than ever. As the market for wind energy grows, wind turbines and wind farms are growing as well. Current utility-scale wind turbines extend to a significant distance into the atmospheric boundary layer (ABL), with rotor diameters of up to 120 meters (m) and 5 megawatts (MW) installed power [48]. To design and control superior performing, less maintenance-

intensive wind farms, the interaction between the ABL, the turbines, and their wakes needs to be better understood. In the past years, wind turbine aerodynamics research has focused on acquiring high-quality experimental data and solving the incompressible Navier-Stokes equations for individual and clustered wind turbines. Often, actuator models are used to reduce grid requirements and simplify the problem. Actuator models are the subject of this thesis. The actuator disk model (ADM) represents the wind turbines as disks that impose body forces on the flow field depending on the fluid velocities. Several variations of the model exist, with some models taking only the axial direction of the imposed force into account and others taking only the axial and tangential forces into account. The actuator line model (ALM) represents the blades as a set of points along each blade axis that rotate in time. Each point defines a discrete section of the blade with its respective airfoil characteristics. The lift and drag forces on the blades are calculated based on the local velocities at each point [49].

2.2 Wind Turbine Aerodynamics

Wind turbines generate power by extracting kinetic energy from the wind. The following analysis is based on One-dimensional Momentum Theory [49]. The air that passes through the turbine is contained within a stream tube. As the power is extracted the wind expands, thus increasing the cross-sectional area of the stream tube. The energy extracting device for this simple model is called an actuator disc. By definition, the mass of air passing through the stream tube is conserved. The air velocity at the disc is related to the free stream velocity by means of the induction factor

$$U_d = U_\infty(1-a) \tag{2.1}$$

where

U_d is the velocity at the disc,

U_∞ is the free stream velocity,

a is the induction factor.

The momentum theory applied to a one-dimensional stream shows that power extracted from the wind is given by

$$C_p = \frac{P}{\frac{1}{2}\rho U_\infty^3 A} = 4a(1-a)^2 \tag{2.2}$$

where

P is power,

ρ is density,

A is the area of the disc.

The power coefficient, C_p, is defined as the ratio of power extracted to the available power in the mean flow. Taking the derivative of C_p with respect to a allows us to find the maximum value of the function. This results in an induction factor of $a = 1/3$ and a maximum power coefficient of $C_p = 16/27 = .593$, which is known as the Betz limit [50](See Appendix B).

Angular momentum theory, which takes into account the rotation of the wake, can be used to obtain the same result [51]. The thrust coefficient is another important parameter and is defined as

$$C_T = \frac{T}{\frac{1}{2}\rho {U_\infty}^2 A} = 4a(1-a) \tag{2.3}$$

where

T is thrust.

As the wind passes through the rotor, an aerodynamic thrust and torque are produced in the blades, which are used then to produce power. The air experiences an equal and opposite force. The increase in kinetic energy of the air due to the force exerted by the blades is compensated by a decrease in pressure. The circulation generated at the blades generates root and tip vortices. These vortices convect downstream with the local flow velocity. The vortex cylinder theory takes into account the spin of the wake, yielding a lower power coefficient. The vortex theory, even though it does not account for wake expansion, produces results that agree with the momentum theory [49].

Blade-element momentum (BEM) theory assumes that the forces on the blade sections may be calculated from two-dimensional (2D) airfoil data. The airfoil lift and drag coefficients are functions of the angle of attack. Wind velocity is a combination of the velocity of the wind, which accounts for axial and tangential induction, and the rotation of the rotor. BEM momentum theory states that the force exerted at each blade element is responsible for the change of momentum in the air that passes through the annulus which is swept by the element [50]. BEM theory yields results for the power coefficient as a function of tip speed ratio.

For heavily loaded turbines, the momentum theory has to be modified because of the creation of a turbulent wake. This causes a mixing process between the wake and the free stream. This mixing process re-energizes the lower energy air that has gone through the rotor.

These basic concepts are used to develop models and techniques to simulate wind turbines inside numerical codes. Simulations provide results not only for the parameters affecting the turbines such as thrust and torque, but also the properties of the wake formed behind the turbine.

2.3 Wind Turbine Computational Fluid Dynamics

In past years, wind turbine computational fluid dynamics (CFD) have been focused on solving the incompressible Navier-Stokes equations [52]. The flow in wind turbines is incompressible with velocities ranging from 5 to 25 meters (m) / seconds (s). Compressibility effects are only present at the tip because of the high velocities caused by rotation. Mach number at the tip is still fairly low ($M <= 0.25$) so it is reasonable to assume that the flow is incompressible, even if resolving the blades. Thus the incompressible Navier-Stokes equations

$$\nabla \cdot \boldsymbol{u} = 0 \tag{2.4}$$

$$\frac{\partial \boldsymbol{u}}{\partial t} + (\boldsymbol{u} \cdot \nabla)\boldsymbol{u} = -\frac{1}{\rho}\nabla p + \nu \nabla^2 \boldsymbol{u} \tag{2.5}$$

are suitable for wind turbine modeling. When dealing with ABL flows, the Boussinesq approximation is typically used for buoyancy effects and an equation for temperature has to be solved. The Coriolis effect may be present when dealing with large wind turbines and wind farms. For ABL flows, the largest scales are on the order of 1 kilometer (km) while the smallest scales are on the order of 1 mm. This disparity of scales makes the option of using direct numerical simulations (DNS) not feasible because of the computational resources required. Researches have adopted Reynolds-averaged Navier-Stokes (RANS) methods to

solve the mean flow. The RANS equations:

$$\frac{\partial \overline{\boldsymbol{u}}}{\partial t} + (\overline{\boldsymbol{u}} \cdot \nabla)\overline{\boldsymbol{u}} = -\frac{1}{\rho}\nabla p + \nu \nabla^2 \overline{\boldsymbol{u}} - \nabla \cdot (\overline{u'u'}) \tag{2.6}$$

are used where over bar denotes Reynolds decomposition $\boldsymbol{u} = \overline{\boldsymbol{u}} + u'$,

and $\overline{u'u'}$ is the Reynolds stress tensor, which is then modeled in terms of the mean flow quantities.

Researchers in the wind energy wake community have adopted large eddy simulations (LES) in recent years. The flow over wind turbines is highly unsteady and, with the RANS equations, these unsteady features are lost due to averaging. A better approach is to use LES, in which the flow dependence in time is resolved. LES calculates the larger eddies while smaller eddies are modeled. The filtered incompressible Navier-Stokes equations used are

$$\frac{\partial \tilde{\boldsymbol{u}}}{\partial t} + (\tilde{\boldsymbol{u}} \cdot \nabla)\tilde{\boldsymbol{u}} = -\frac{1}{\rho}\nabla \tilde{p} + \nu \nabla^2 \tilde{\boldsymbol{u}} - \nabla \cdot (\widetilde{uu} - \tilde{u}\tilde{u}) \tag{2.7}$$

where the term $(\widetilde{uu} - \tilde{u}\tilde{u})$ is often modeled by:

$$\tau_{SGS} = \widetilde{uu} - \tilde{u}\tilde{u} = -\nu_{SGS}(\nabla \tilde{u} + (\nabla \tilde{u})^T) \tag{2.8}$$

and ν_{SGS} is the subgrid-scale (SGS) viscosity and is modeled using several subgrid-scale models. The filtering operation was applied at $u = \tilde{u} + u''$.

In past years, RANS and LES have been used to simulate wind turbine flow [49].

2.4 Turbulence Modeling

Concerning the study of viscous flows, a laminar regime exists only at low *Reynolds number*

$$Re = \frac{\rho U L}{\mu} \tag{2.9}$$

where L is a characteristic length scale (e.g. the chord length for airfoil sections), U the undisturbed stream velocity and μ the dynamic viscosity. The Reynolds number represents the inertial (i.e. convective) to viscous forces ratio. Indeed, when the Reynolds number growths, the flow field structures change and time-fluctuating velocity and pressure components appear, even though boundary conditions are still steady in a time-averaged sense. When the flow regime becomes turbulent, the fluid motion looks disorganized and single particles follow a winding path. This being even if the mean are well-established paths, which is properly defined as main stream flow. A turbulent flow has often high level vorticity, which means also that diffusion phenomena come out for all the physical properties of the flow, both vector (e.g. momentum) and scalar (e.g. temperature)[16].

For the prediction of wind turbine aerodynamics, both of the Spalart-Allmaras and k–ω SST turbulence models can be repeatedly found in the literature. However, k–ω SST turbulence model furthermore is generally retained as the most proper solution for this specific issue (see e.g. [53–55]).

2.4.1 k–ω SST

k–ω model is one of the most commonly used models. This include two additional transport equations to represent turbulent properties of flow to account for history effects like convection and diffusion of turbulent energy. The transport variable

k determines the energy in turbulence and ω determines the scale of turbulence [56, 57].

In the k–ω turbulence models the transport equation of the turbulent kinetic energy is solved together with the equation of the specific rate of dissipation of turbulent kinetic energy, defined as $\omega = \epsilon/k$. This model performs well with free shear flows, flat plate boundary layer flows, complicated adverse pressure gradient flows and separated flows. A problem of the standard k–ω model is the dependency on the free stream boundary conditions. The shear-stress transport (SST) k–ω model was developed by Menter [58–60] to effectively blend the robust and accurate formulation of the k–ω model in the near-wall region with the free-stream independence of the k–ϵ model in the far field. The SST k–ω model is similar to the standard k–ω model, but includes a number of features that make the SST k–ω model more accurate and reliable for a wider class of flows (e.g., adverse pressure gradient flows, airfoils, transonic shock waves) than the standard k–ω model. The SST k–ω model equations read [61, 62]

$$\frac{\partial}{\partial t}(\rho k) + \frac{\partial}{\partial x_i}(\rho k u_i) = \frac{\partial}{\partial x_j}(\Gamma_k \frac{\partial k}{\partial x_j}) + \widetilde{G}_k - Y_k + S_k \tag{2.10}$$

$$\frac{\partial}{\partial t}(\rho \omega) + \frac{\partial}{\partial x_i}(\rho \omega u_i) = \frac{\partial}{\partial x_j}(\Gamma_\omega \frac{\partial \omega}{\partial x_j}) + G_\omega - Y_\omega + D_\omega + S_\omega \tag{2.11}$$

In these equations, the term $\widetilde{G}_k$ represents the generation of turbulence kinetic energy due to velocity gradients and is defined in the same manner as in the standard k–ω model. G_ω represents the generation of ω , calculated as described for the standard k–ω model in Modeling the Turbulence Production [62]. Γ_k and Γ_ω represent the effective diffusivity of k and ω, respectively. Y_k and Y_ω represent the dissipation of k and ω, respectively, due to turbulence, calculated as described

in Modeling the Turbulence Dissipation [62]. D_ω represents the cross-diffusion term while S_k and S_ω are user-defined source terms.

2.4.2 The Finite Volume Method

OpenFOAM as well as the commercial code Fluent solve the governing integral equations for the conservation of mass and momentum, and (when appropriate) for energy and other scalars, such as turbulence and chemical species [61,63]. In both cases a control-volume-based technique is used [64,65], which consists of:

- Division of the domain into discrete control volumes using a computational grid.
- Integration of the governing equations on the individual control volumes to construct algebraic equations for the discrete dependent variables (unknowns),such as velocities, pressure, temperature, and conserved scalars.
- Linearizion of the discretized equations and solution of the resultant linear equation system, to yield updated values of the dependent variables.

This page is intentionally left blank.

Chapter 3

Fluid-Structure Interaction

Contents

3.1 Introduction

This chapter shows the performed fluid-structure interaction (FSI) study on the horizontal axis wind turbine rotors. Firstly, pre-computational study was done on the wind turbine airfoil DU96-W-180. That study yielded some important

parameters to consider in the following simulations like the turbulence model and the appropriate mesh sizing to capture the physical behavior of the flow at near-stall angles of attack. Next, a vortex-based method for FSI simulations was discussed showing some sample results on the NREL 5MW HAWT rotor. Afterwards, CFD-based method was introduced for FSI simulations showing various aerodynamic and structural properties of the NREL 5MW HAWT rotor. Finally, for the sake of validation, a comparison between various codes were carried out showing a good agreement and useful suggestions for future extension of this work.

Today, industrial design codes for wind turbine rotors are still based on BEM [47, 53]. Nevertheless, in the last decade the opinion has been advanced that aerodynamic modeling of HAWT rotors by means of the conventional engineering methods has reached a point where no further improvement can be expected without a full understanding of the flow physics [66]. Thus, the last years have seen the rise of numerical studies on all HAWT aerodynamics features, performed on many different levels, ranging from BEM methods integrated by CFD calculations, to full 3D Navier-Stokes models. Many authors have used the generalized Actuator Disk Method, which represents roughly an extension of the BEM method, integrated in a Euler or NS frame [67, 68]. To overcome its main limitation, i.e. the forces are distributed evenly along the actuator disk in the azimuthal direction, a 3D N-S solver has been combined with the so-called Actuator Line Technique, in which the loading is distributed along lines representing the blade forces [6, 47, 67]. In the few past years, Sankar and co-workers [55, 69–71] developed a hybrid Navier-Stokes/Full-Potential/Free Wake Method, mainly for predicting 3D viscous flow over helicopter rotors and then extended it to the HAWT flow field. The computational domain is divided into different region, each one is solved by the proper approach: N-S solution near the blades, potential flow representation on the outer

field, and a collection of vortex methods for the vorticity field modeling [16].

3.2 Aerodynamics Precomputations

3.2.1 Model Description

In these simulations, the flow is assumed two-dimensional, incompressible at high Reynolds Number (Re). The flow simulations around DU96-W-180 airfoil whose profile is shown in Fig. 3-1 are done with the geometrical and air flow parameters summarized in Table 3.1. The numerical simulations were computed using a 20-core Linux cluster using OpenFOAM's, unsteady incompressible solver; pisoFoam and k–ω SST turbulence model was chosen for this simulation.

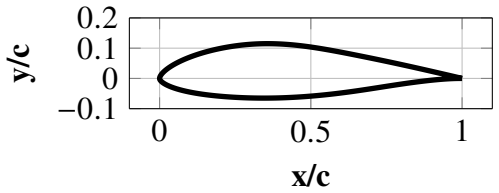

Figure 3-1: Profile of DU-96-W-180 airfoil.

Table 3.1: A list for the basic flow and airfoil parameters.

Symbol	Value	Unit
α	10	$[^o]$
Re	0.7×10^6	$[-]$
μ_{air}	1.789×10^{-5}	$[kg/(m\,sec.)]$
ρ_{air}	1.225	$[kg/m^3]$
ν_{air}	1.461×10^{-5}	$[m^2/sec.]$

3.2.2 Mesh Description and Case Setup

A 2D dense mesh was constructed around a DU96-W-180 airfoil using ANSYS ICEM CFD as shown in Fig. 3-2. The mesh is an unstructured C-grid extending

from 5 chords upstream to 10 chords downstream. It is split into 8,220 quad-elements and 139,989 tri-elements with stats as follows [points: 157,510, faces: 523,382, internal faces: 225,883, cells: 148,209, faces per cell: 5.05546]. Fig. 3-2 shows also a special mesh refinement that was done to fit the boundary layer near the airfoil wall.

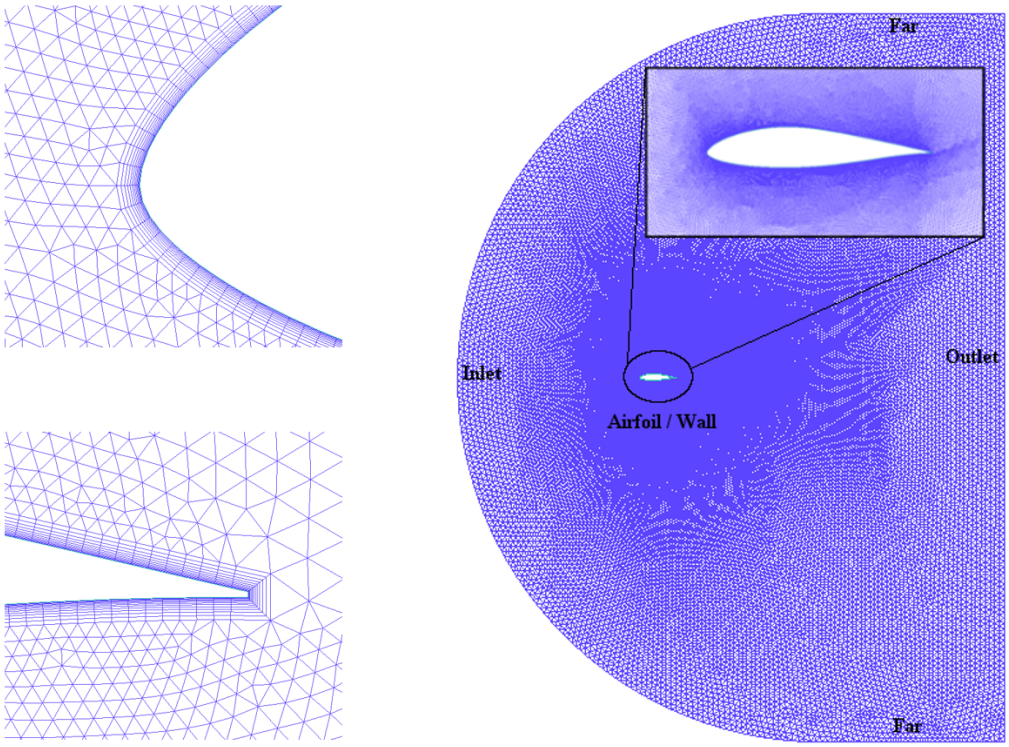

Figure 3-2: The constructed mesh around DU96-W-180 airfoil with the boundary conditions patches.

The boundary conditions of the problem are defined along 5 patches as shown in Fig. 3-2. The pressure is zeroGradient everywhere except for the outlet where its value is known to be atmospheric pressure. However, for the velocity, it's fixedValue and equal to the uniform freestream value at the inlet and the far boundaries, calculated for the outlet while for the wall boundary, it reduces to zero (due to no-slip condition). The chosen solver is pisoFoam which is used to

solve incompressible unsteady flow by a PISO algorithm with a generic turbulence model option (in this case: k–ω SST).

3.2.3 Results

In this section, simulations are shown for the flow around the wind turbine airfoil DU96-W-180 airfoil. The computations were carried on till the complete unsteady Kármán vortex shedding is formed in the airfoil's downstream flow. The velocity distribution is shown in Fig. 3-3.

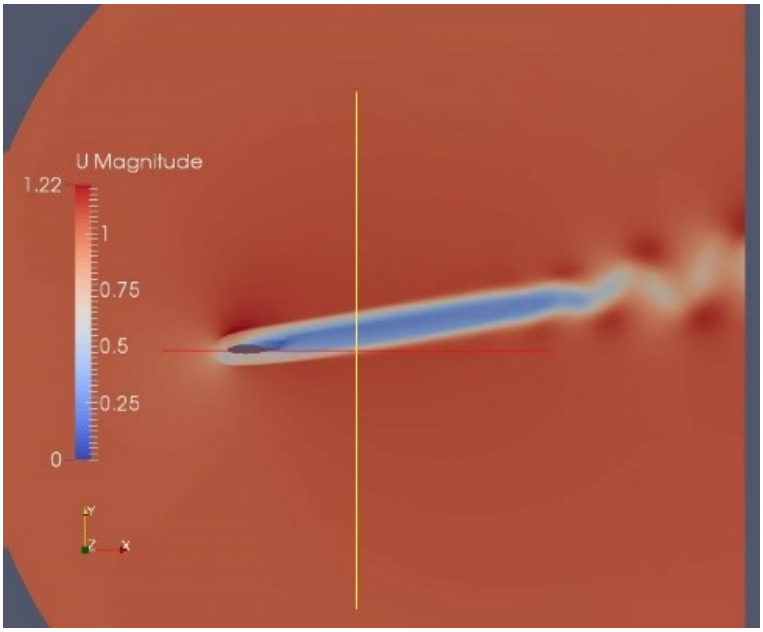

Figure 3-3: The velocity distribution around the airfoil showing the unsteady Kármán vortex shedding.

Based on the experimental results obtained by Timmer [91] shown in Fig. 3-4., the maximum lift coefficient was found to be close to 10 degrees. Thus, in this work simulations were carried on until 10 degrees. As shown in Fig. 3-5., the numerical lift coefficient distribution agrees very well with the experimental data.

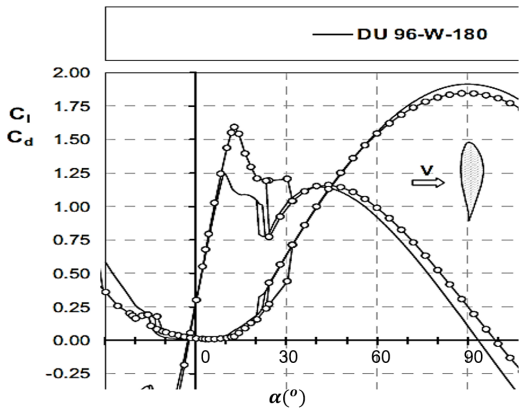

Figure 3-4: The experimental performance of DU96-W-180 with the angle of attack by Timmer [91].

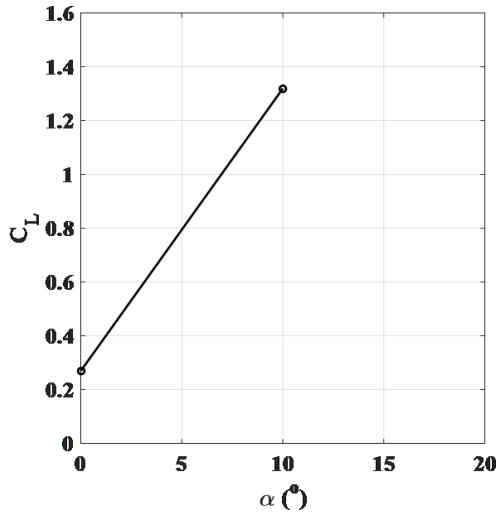

Figure 3-5: The numerical performance of DU96-W-180 with the angle of attack.

At an angle of attack of 10 degrees, the numerical C_L value is about 1.31, yet it's around 1.25 experimentally. Thus, OpenFOAM's pisoFoam solver alongside the k–ω SST turbulence model solver was able to successfully capture stall characteristics with a reasonable error of 4.8%. To capture post-stall aerodynamic characteristics, further simulations beyond 10 degrees were carried on, however they were quite challenging for the current conditions.

3.3 Fluid-Structure Interaction

3.3.1 Vortex-Based Method

3.3.1.1 Model Description

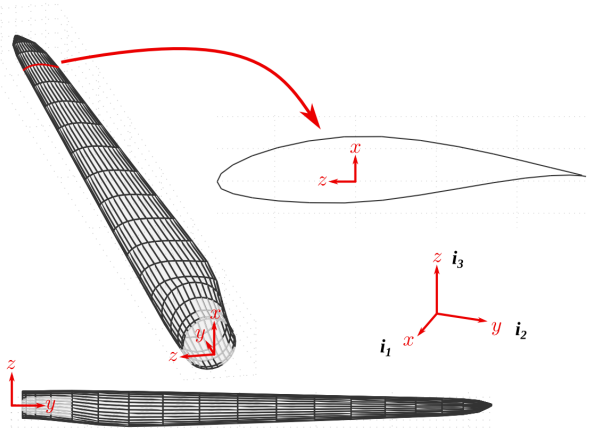

Figure 3-6: MIRAS blade coordinate system [25].

MIRAS is a 3D viscous–inviscid interactive solver for HAWT rotor computations. The solver predicts the aerodynamic behavior of wind turbine wakes and blades for steady and unsteady conditions. The MIRAS code consists of inviscid and viscous parts. The inviscid part is a 3D panel method using a surface distribution of quadrilateral sources and doublets [25].

The inviscid part is coupled to the viscous part through the integral viscous boundary layer solver, Q^3UIC [72]. Transpiration velocity data from Q^3UIC is used to modify the inviscid solution from MIRAS and take the viscous effects into account. A free-wake model simulates the wake behind the wind-turbine rotor using vortex filaments that carry the vorticity shed by the blades trailing edges. The MIRAS free-wake model under varying conditions. A particle mesh implementation as described in [73] is used in the current paper for improved computational efficiency. The MIRAS code is parallelized using message passing interface (MPI)

software from Oracle Solaris Studio version 12.3 [25, 74].

FLEX5 is an aeroelastic program developed by Øye [26] to model the dynamic behavior of HAWTs operating in specified wind conditions such as simulated turbulent wind. The program runs in the time domain producing time series of loads and deflections. Aerodynamics are calculated using the BEM method with additional models important for unsteady and yaw and/or tilt conditions. Such models include dynamic wake and dynamic stall, see, e.g., Øye [75], Schepers and Snel [76] and Snel and Schepers [77]. The structural behavior of the wind turbine is modeled using the principle of virtual work and carefully selected degrees of freedom (DOFs). Modal shape functions are used for the deflections of the blades and tower, while stiff bodies connected by flexible hinges model the nacelle, rotor shaft and hub. FLEX5 contains a total of 28 DOFs where six of the 28 DOFs describe the deformations of a flexible foundation. In the present paper, only a maximum of 22 of the 28 DOFs are considered. The six DOFs that describe motions of the foundation for offshore applications are excluded.

For more details about the coupling techniques and the methodology involved in MIRAS-FLEX, see Appendix D.

3.3.1.2 Results

Simulations were performed on the reference NREL 5MW HAWT in an upwind configuration using the MIRAS-FLEX FSI code [25]. The inlet flow velocity is 10 m/s and rotor the angular velocity is 1.2 rad/s. The simulation was performed using 208 parallel cores of KU HPC server.

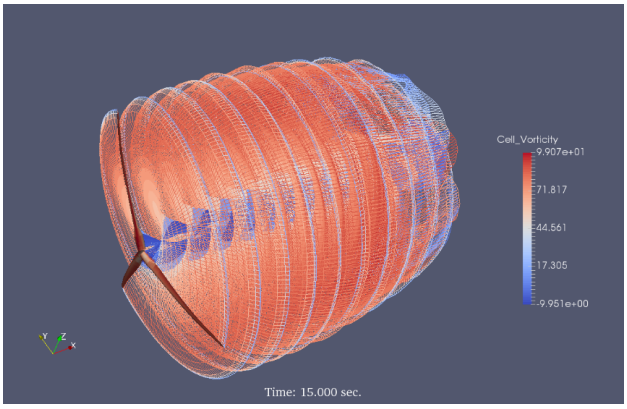

Figure 3-7: Wake progression of the NREL 5MW HAWT using MIRAS-FLEX.

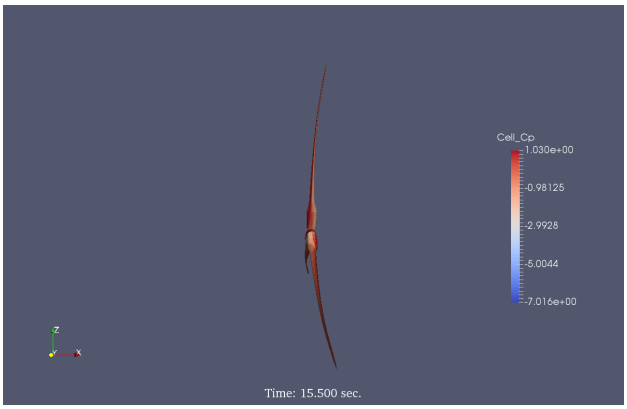

Figure 3-8: Out-of-plane aeroelastic bending effect on the NREL 5MW HAWT using MIRAS-FLEX.

Further results are shown in the next section in comparison with the CFD-based method and the other BEM-based codes.

3.3.2 CFD-Based Method

3.3.2.1 Model Description

In this section, a steady-state 1-way FSI analysis was performed to get the aeroelastic response due to the aerodynamic loading on NREL 5MW reference HAWT blade. The blade characteristic geometry data was based on previous literature

data from Bazilevs et al. [24] and Sessarego et al. [25]. Firstly, the pressure loads on the blade surface were computed using Ansys Fluent then passed on to Ansys Mechanical to compute the stresses and deformations on the blade. The blade had a length of 63 m and a pitch angle at the tip of 0 degrees. Due to the symmetry of the turbine rotor, shown in Figure 3-9 and to save the computational cost and time, a single blade only was considered for this simulation with periodic/cyclic boundary conditions to account for the other two blades similarity in a rotational manner.

3.3.2.2 Mesh Description and Case Setup

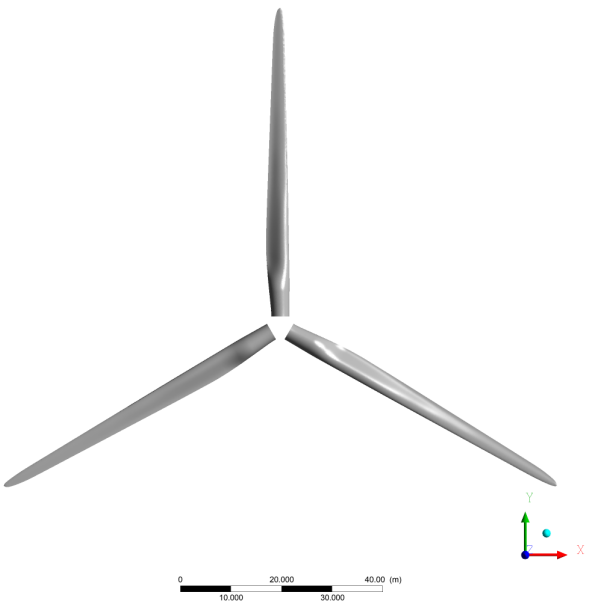

Figure 3-9: The NREL 5 MW wind turbine rotor [24].

In order to apply the CFD solver to the problem, a sizable fluid domain needed to be defined around the blade extending far enough upstream and downstream.

Afterwards, that domain needed to be discretized reasonably to capture the physical properties of the flow around the turbine as well as the mutual interaction with the surfaces. Consequently, a large domain was constructed around the blade as shown in Figure 3-10 accounting for the downstream wake shedding. A domain sensitivity study was done using various meshes from coarse to fine ones with different number of elements to guarantee mesh-independent solutions. Finally, the chosen domain and mesh specifications are shown in detail as follows.

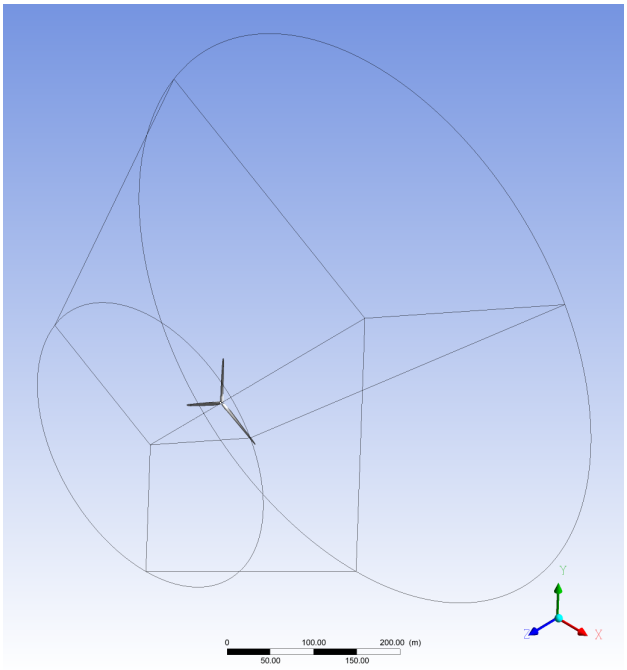

Figure 3-10: The mesh domain boundaries around the NREL 5 MW HAWT rotor.

A dense unstructured mesh was constructed around that blade with 14,958,918 hybrid cells and $3,962,585$ nodes with clustered density around the blade region as shown in Figure 3-11. A special refined structured layers were generated near the blade surface to capture the boundary layer properties and viscous effects as shown in Figure 3-12.

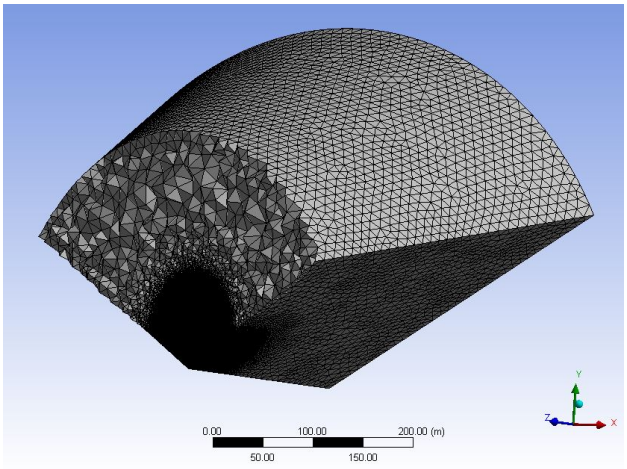

Figure 3-11: A sectional view of the constructed fluid mesh around the NREL 5 MW HAWT blade.

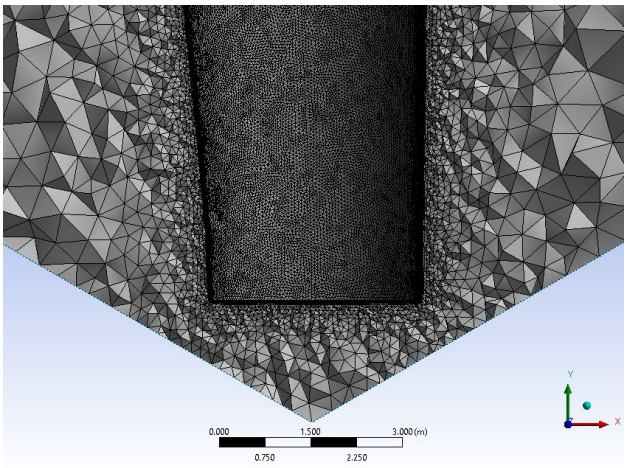

Figure 3-12: A close-up view of the refined mesh near the NREL 5 MW HAWT blade surface.

The mesh quality was checked to ensure the accuracy of the solution. The average orthogonality quality was found to be 0.79128 with a standard deviation of 0.11992 as shown in Figure 3-13, which is very reasonable. Moreover, the mesh skewness quality was found to be 0.20763 with a standard deviation of 0.12074 as shown in Figure 3-14, which is very acceptable too.

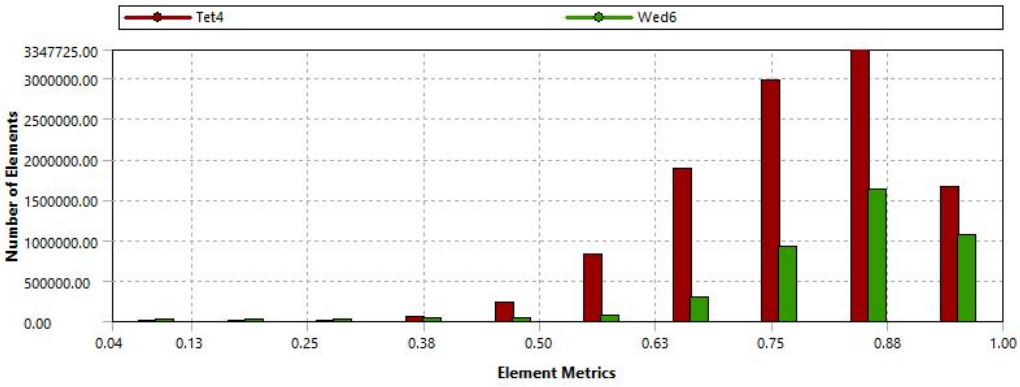

Figure 3-13: Orthogonality quality of the constructed fluid mesh.

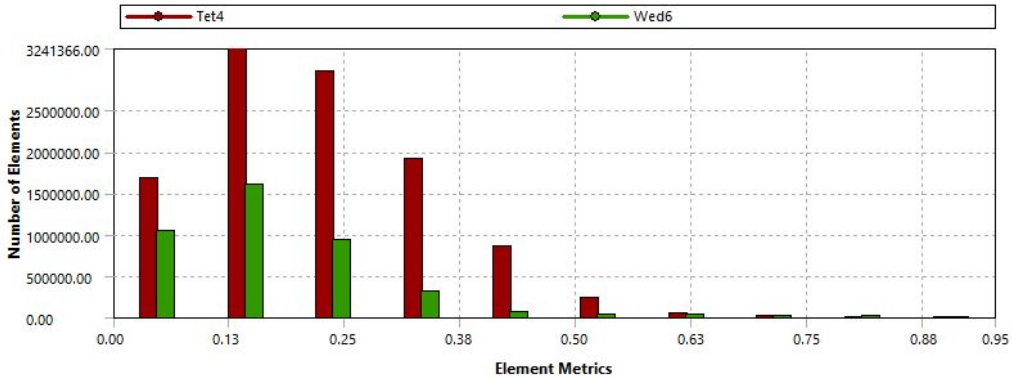

Figure 3-14: Skewness quality of the constructed fluid mesh.

In preparation for the structural part of the solver, a reasonable surface mesh is required for the blade before proceeding to the finite element analysis. Figure 3-15 depicts the constructed mesh on the NREL 5 MW blade surface. The mesh is structured with 5,635 elements and 5,639 nodes. Besides, to guarantee enough accuracy of the solution, the mesh metrics were calculated and shown as follows. Figures 3-16 and 3-17 shows the orthogonality and skewness quality of the constructed structural mesh, respectively. It's obvious that both of them show very acceptable metrics to achieve solutions with good enough accuracy.

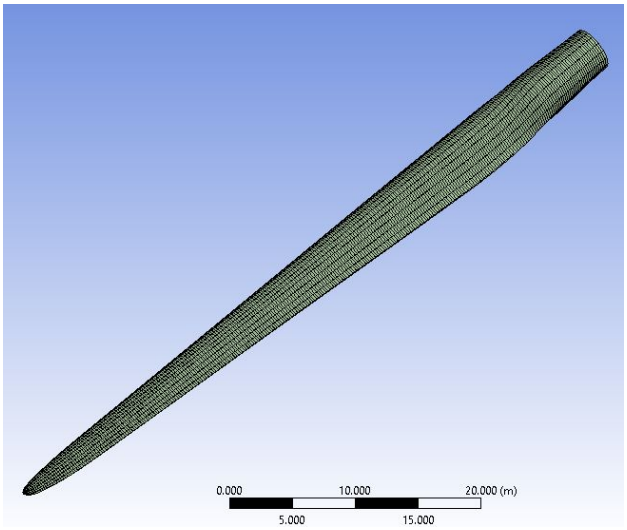

Figure 3-15: The constructed structural mesh on the NREL 5 MW HAWT blade.

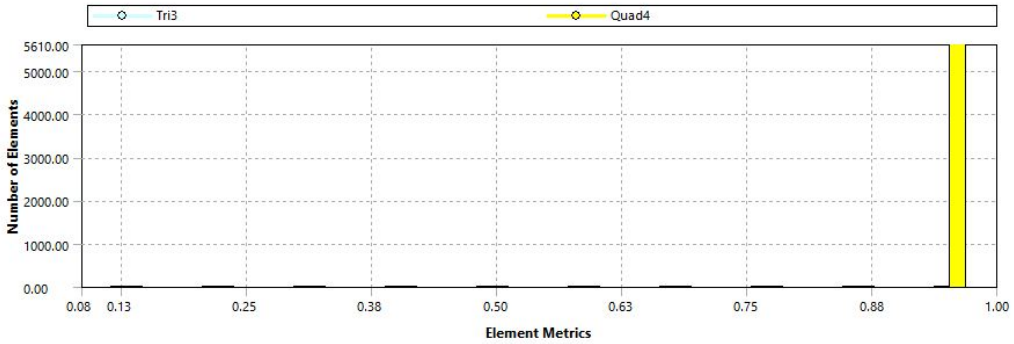

Figure 3-16: Orthogonality quality of the constructed structural mesh.

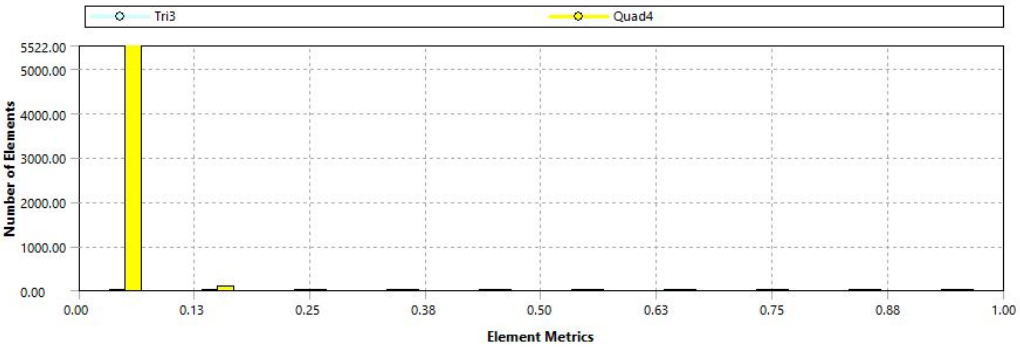

Figure 3-17: Skewness quality of the constructed structural mesh.

3.3.2.3 Results

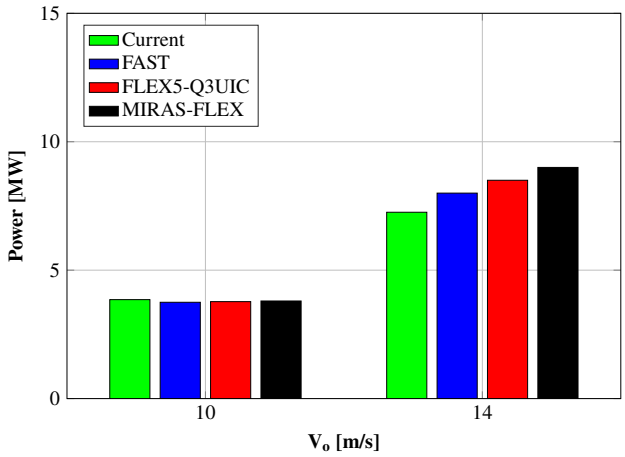

Figure 3-18: Aerodynamic Power versus wind speed, V_o , for comparison between the current simulation, FAST, FLEX5-Q^{3}UIC, and MIRAS-FLEX.

In this section, the results of the test cases will be shown and validated against DTU's MIRAS-FLEX results as well as the BEM-based FLEX5-Q^{3}UIC and FAST codes [25]. DTU's MIRAS-FLEX is a coupled aeroelastic code that is based on a three-dimensional viscous–inviscid method for wind turbine computations. The case study for this work is based on the test case #2 of Sessarego et al. [25]. The inflow is steady and uniform wind tested at speeds of 10 m/s and 14 m/s. The tip speed ratio (TSR) is fixed at 7.55 up to the maximum rotor angular speed 12.1 rpm at 10 m/s. For the 14 m/s wind speed, the rotor angular speed is fixed at 12.1 rpm allowing for a decrease in the tip-speed ratio with the increased wind speed. For this specific case, the blade pitch angle is specified at a value of zero and fixed for all wind speeds. The pitch regulations had been discarded at the rated power, since it was more interesting to observe the stall behavior of MIRAS-FLEX and its comparison to FLEX5 and FAST as explained in detail by Matias et al [25]. Furthermore, zero values were assigned to the tower shadow, tilt angle and gravity to achieve non-oscillating loads [25]. The solver is applied using k-ω SST model

to account for the turbulence effects. Moreover, the computations were run on the Kyushu University multi-core Linux cluster using the public domain openMPI implementation of the standard message passing interface (MPI).

In order to check the output power of this rotor, the generated torque by the rotor was firstly calculated and then multiplied by the rotational speed of the rotor. For the first case of 10 m/s wind speed and 11.4 RPM, the rotor torque was found to be 3221.85 $kN.m$ which matches well the FAST, FLEX5-Q^{3}UIC, and MIRAS-FLEX codes values which are roughly clustered around 3200 $kN.m$. Similarly, for the second case of 14 m/s wind speed and 12.1 RPM, the rotor torque was found to be 5725.74 $kN.m$ which is very comparable to those of FAST, FLEX5-Q^{3}UIC, and MIRAS-FLEX codes.

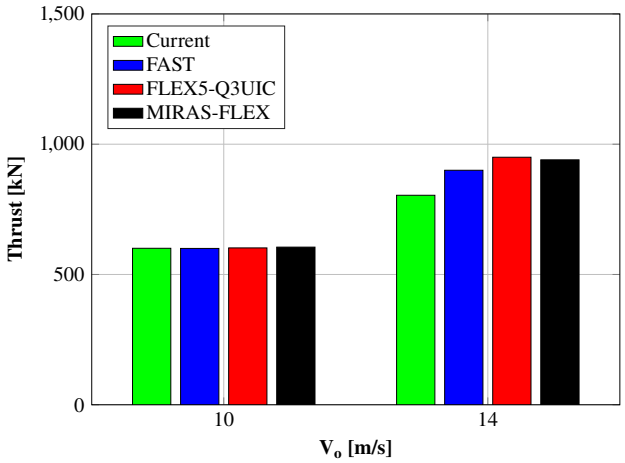

Figure 3-19: Aerodynamic Thrust versus wind speed, V_o , for comparison between the current simulation, FAST, FLEX5-Q^{3}UIC, and MIRAS-FLEX.

Figures 3-18 and 3-19 shows the comparison between the current simulation and the other codes for the aerodynamic power and thrust, respectively. The results generally agree well from all codes. However, the slight differences were due to the fact that some of the used airfoil data are based on two-dimensional

polar measurements [78] as in FAST and FLEX5 while they are based on Q^{3}UIC simulations in MIRAS-FLEX.

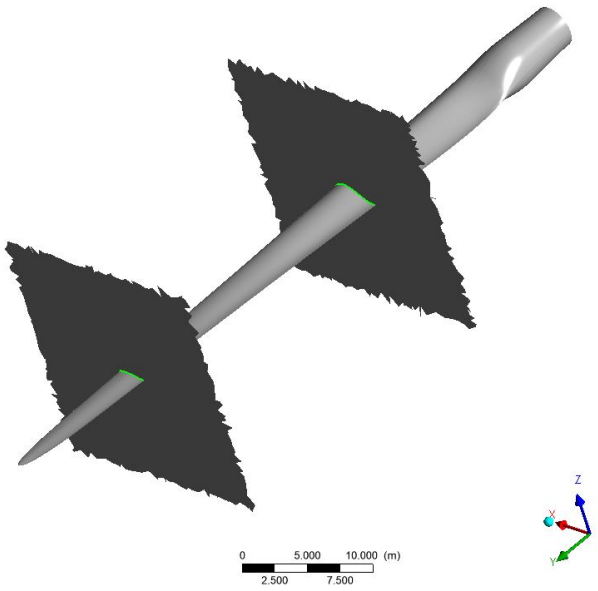

Figure 3-20: The span-wise locations of the cutting planes on the blade.

On the other hand, the loading distribution on the blade in the span-wise direction was achieved by applying two cutting planes to two span-wise stations $r/R = 0.4$ and $r/R = 0.8$ as shown in Figure 3-20. The extracted aerodynamic loads which are normal to the turbine's rotor plane are depicted in Figures 3-21 and 3-22 for increasing wind speeds and rotor RPM. Besides the tangential loads to the turbine's rotor plane are shown in Figures 3-23 and 3-24 for increasing wind speeds and rotor RPM. The current simulation results agree well with the results from FAST, FLEX5-Q^{3}UIC, and MIRAS-FLEX. The values are quite identical at the first case study at a wind speed of 10 m/s since it's closer to the rated speed. However, for the second case of 14 m/s speed, the values are slightly varying due to the high loads affecting the rotor blades at high speeds. Such high loads yield considerable deflections as will be shown later in the structural results which in

turn induce flow instabilities like air flow stall over the blade surface.

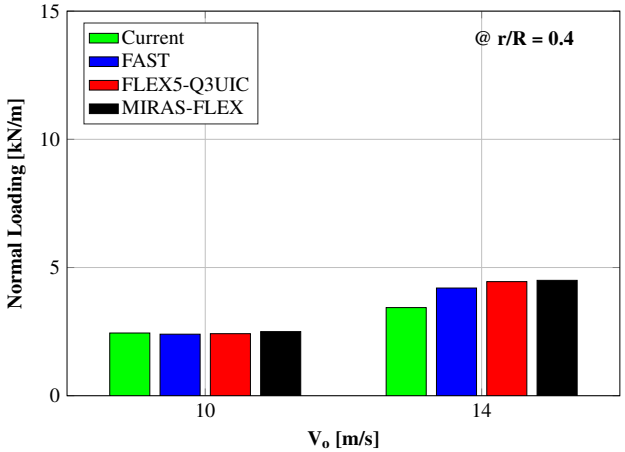

Figure 3-21: Normal loads to the rotor plane comparison between the current simulation, FAST, FLEX5-Q^{3}UIC, and MIRAS-FLEX for increasing wind speeds and rotor RPM at the span-wise location $r/R = 0.4$.

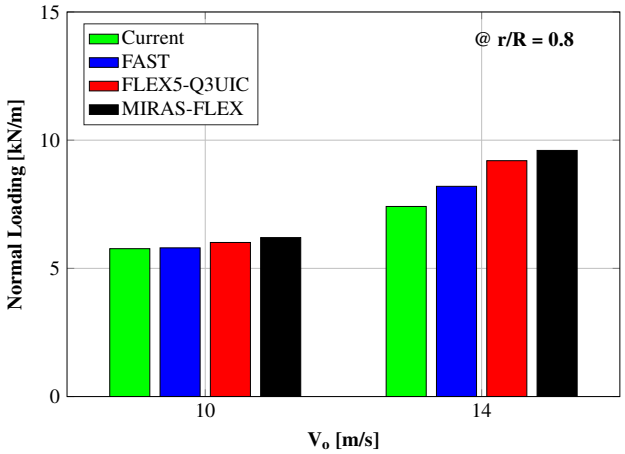

Figure 3-22: Normal loads to the rotor plane comparison between the current simulation, FAST, FLEX5-Q^{3}UIC, and MIRAS-FLEX for increasing wind speeds and rotor RPM at the span-wise location $r/R = 0.8$.

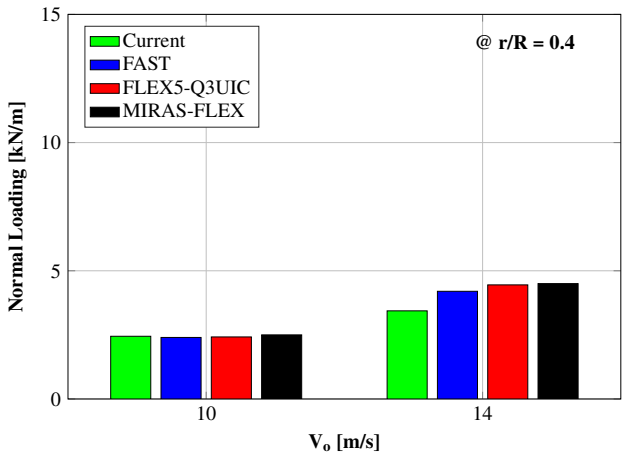

Figure 3-23: Tangential loads to the rotor plane comparison between the current simulation, FAST, FLEX5-Q^{3}UIC, and MIRAS-FLEX for increasing wind speeds and rotor RPM at the span-wise location $r/R = 0.4$.

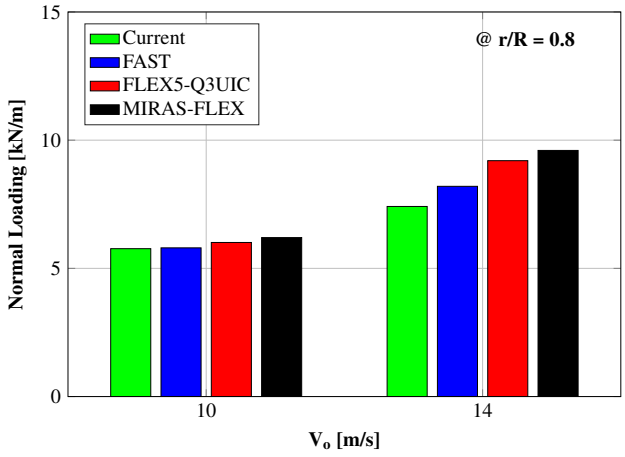

Figure 3-24: Tangential loads to the rotor plane comparison between the current simulation, FAST, FLEX5-Q^{3}UIC, and MIRAS-FLEX for increasing wind speeds and rotor RPM at the span-wise location $r/R = 0.8$.

In order to visualize and justify the occurrence possibility of flow instabilities, the blade local velocity distribution was plotted at two span-wise stations $r/R = 0.4$ and $r/R = 0.8$ at different wind speeds as shown in Figures 3-25 to 3-26 and Figures 3-27 to 3-28, respectively. It's obvious that one of the flow instabilities that start to

buildup at higher speeds, is the stall over the blade surface. As shown in Figures 3-26 and 3-28, the flow starts to separate from the blade surface causing the stall phenomenon to build up. Consequently, it's necessary to propose some promising solution for this crucial problem as will be seen in the following chapter.

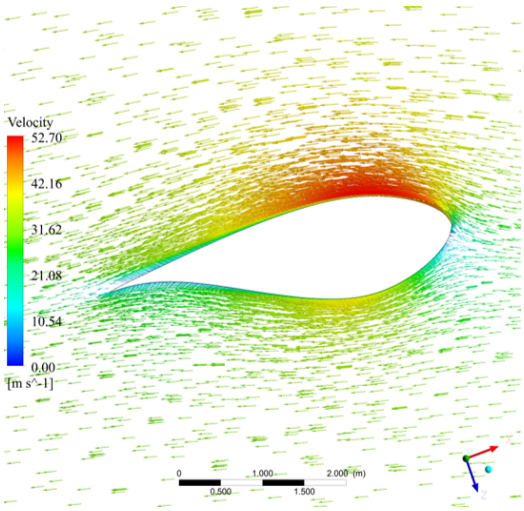

Figure 3-25: Local CFD velocity distribution for the NREL 5MW HAWT blade at the span-wise location: $r/R = 0.4$ and wind speed: $V_o = 10\ m/s$.

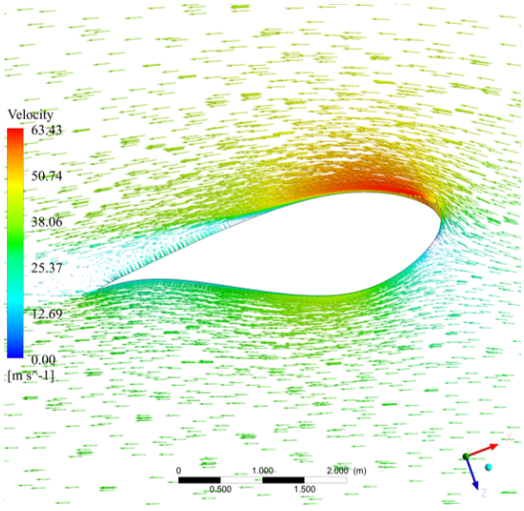

Figure 3-26: Local CFD velocity distribution for the NREL 5MW HAWT blade at the span-wise location: $r/R = 0.4$ and wind speed: $V_o = 14\ m/s$.

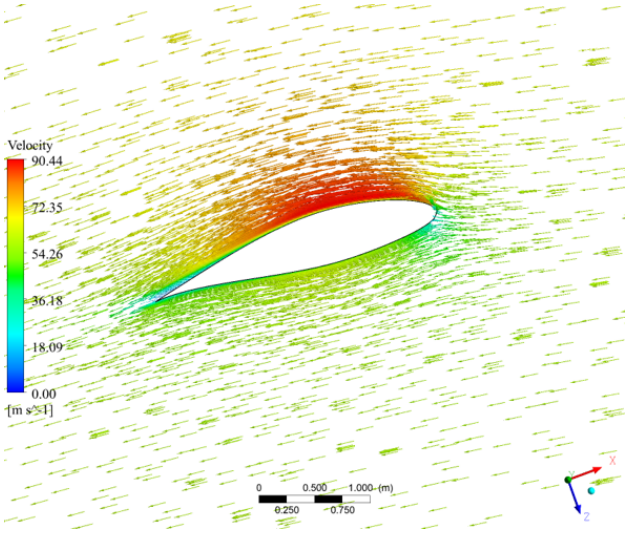

Figure 3-27: Local CFD velocity distribution for the NREL 5MW HAWT blade at the span-wise location: $r/R = 0.8$ and wind speed: $V_o = 10\ m/s$.

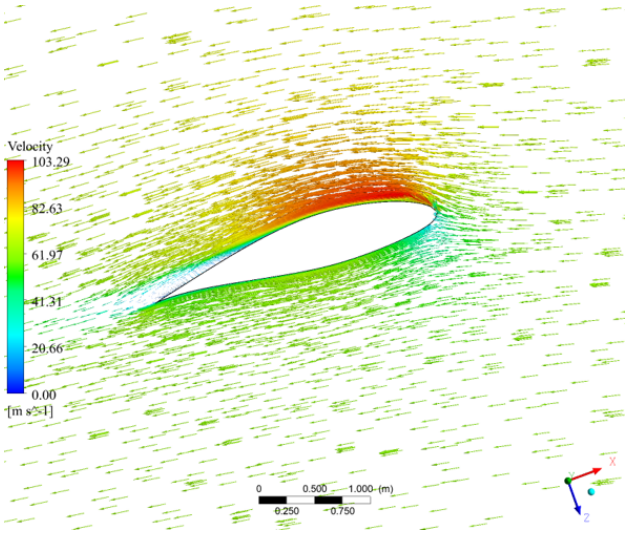

Figure 3-28: Local CFD velocity distribution for the NREL 5MW HAWT blade at the span-wise location: $r/R = 0.8$ and wind speed: $V_o = 14\ m/s$.

Figures 3-29 and 3-30 show the corresponding aeroelastic out-of-plane deflections of the rotor blades for the cases of wind speeds of 10 m/s and 14 m/s, respectively. It's obvious that at higher wind speed the deflection of the blade is larger and consequently inducing more stresses.

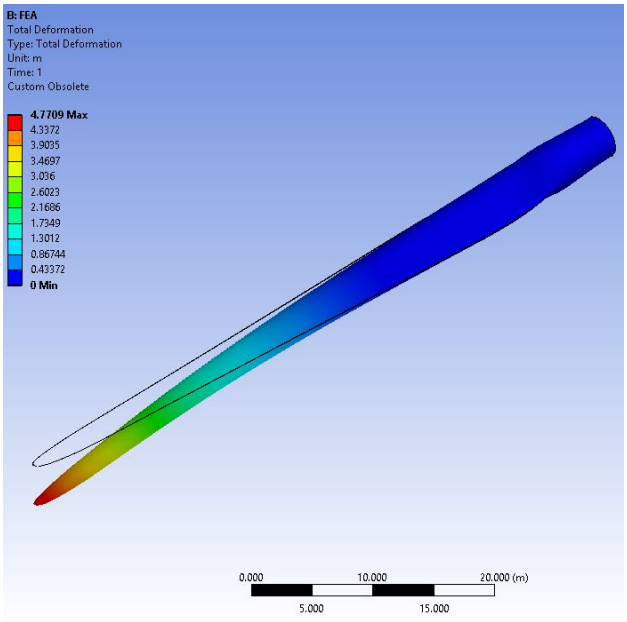

Figure 3-29: Aeroelastic deformation of the NREL 5MW HAWT blade at the wind speed: $V_o = 10\ m/s$.

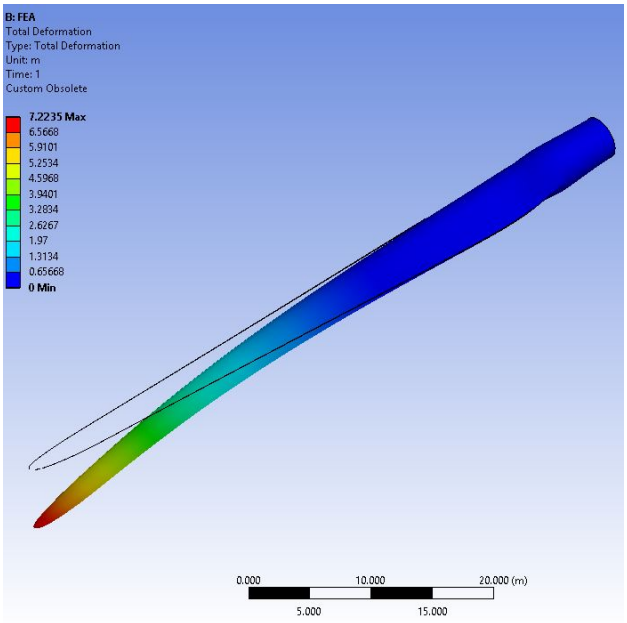

Figure 3-30: Aeroelastic deformation of the NREL 5MW HAWT blade at the wind speed: $V_o = 14\ m/s$.

To validate the results, the resultant tip deflections in both cases were compared against FAST, FLEX5-Q^{3}UIC, and MIRAS-FLEX codes as shown in Figure 3-31. The current simulation values are in good agreement with the other codes values. The results might be slightly higher in the second case of 14 m/s wind speed due to the accumulated slight errors from the aerodynamic part. Besides, an approximated estimate for the structural properties of the blade that were based on the NREL's technical report [79] and Cornell's data [80] was used in the structural part. Such an approximation was necessary to fit the model specifications in the current simulation, though it's acceptable since it yielded reasonable fluid-structure interaction results.

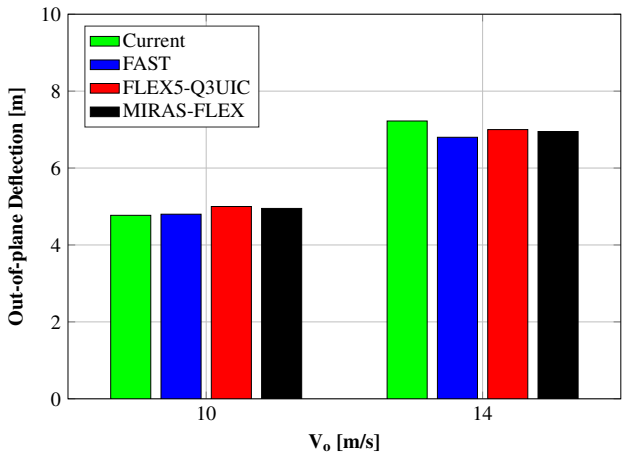

Figure 3-31: Out-of-plane blade tip deflections comparison between the current simulation, FAST, FLEX5-Q^{3}UIC, and MIRAS-FLEX for increasing wind speeds and rotor RPM.

3.4 Summary

This chapter concludes that using k–ω SST turbulence model was an effective choice to appropriately capture this case physical behavior. Besides, the simulations dictate that the mesh sub-viscous layer sizing should be within a yplus value

of 1 for better accuracy. The FSI results from all codes were generally in a very good agreement for both the aerodynamic and structural parts. The results match well near the rated wind speed while slightly vary beyond it due to the inherent instabilities associated with higher wind speeds that needs further study. Besides, the current simulations shows a good prediction for the FSI behavior of the NREL 5MW HAWT rotor which will help developing more complicated solvers in the future. Additionally, it was clear that the current numerical model needs more accurate model at the regime of higher wind speeds. One improvement to be done is though introducing new innovative flow performance enhancement techniques as will be discussed in detail in Chapter 4.

Chapter 4

Active Flow Control

Contents

4.1 Introduction

As discussed in the previous chapter, enhancing the aerodynamic performance of the blades is a critical issue in the development of wind turbines. In this chapter

a new innovative flow performance enhancement technique is presented to solve blade stall issue. An active flow control technique is shown and also its relevant numerical simulations (uncontrolled and controlled). Firstly, the model description is shown for the DU-96-W-180 airfoil as well as the wind flow conditions. Next, the governing equations are summarized in the light of the current assumptions. Afterwards, the constructed mesh, domain definitions and the case setup are shown. The developed flow control solver is also discussed showing the implementation technique. Simulations were done for an incompressible, unsteady air flow over a DU-96-W-180 airfoil using that newly developed OpenFOAM solver. Different actuation frequencies were tested to get the optimum actuation frequency value. Finally the results were recorded and compared as depicted in the following sections.

4.2 Model Description

In these simulations, the flow is assumed two-dimensional, laminar, incompressible, and low *Re* flow. The flow simulations around DU96-W-180 airfoil whose profile is shown in Fig. 4-1 are done with the geometrical and air flow parameters summarized in Table 4.1.

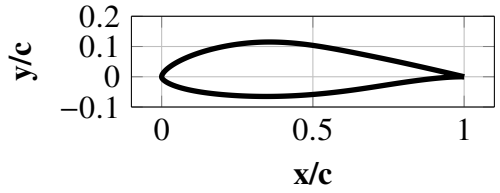

Figure 4-1: Profile of DU-96-W-180 airfoil.

Table 4.1: A list for the basic flow and airfoil parameters.

Symbol	Value	Unit
α	10	$[^o]$
Re	5×10^4	$[-]$
μ_{air}	1.789×10^{-5}	$[kg/(m\,sec.)]$
ρ_{air}	1.225	$[kg/m^3]$
ν_{air}	1.461×10^{-5}	$[m^2/sec.]$

4.3 Governing Equations

In the light of the previous assumptions, the required Navier-Stokes equations to be solved through CFD are simplified to the following incompressible continuity and momentum equations:

$$\boldsymbol{\nabla}\cdot\boldsymbol{U}=0 \tag{4.1}$$

$$\frac{\partial \boldsymbol{U}}{\partial t}+\nabla\cdot(\boldsymbol{U}\,\boldsymbol{U})-\nabla\cdot(\nu\,\nabla\boldsymbol{U})=-\frac{\nabla \boldsymbol{p}}{\rho} \tag{4.2}$$

where, $\boldsymbol{U}$ is the velocity vector, while $\boldsymbol{p}$ is the pressure field. These equations were implemented within OpenFOAM®'s *pisoFoam* solver using the PISO algorithm.

4.4 Mesh Description and Case Setup

A 2D dense mesh was constructed around a DU96-W-180 airfoil using ANSYS ICEM CFD as shown in Fig. 4-2. The mesh is an unstructured C-grid extending from 5 chords upstream to 10 chords downstream. It is split into 8,220 quad-elements and 139,989 tri-elements with stats as follows [points: 157,510, faces: 523,382, internal faces: 225,883, cells: 148,209, faces per cell: 5.05546]. Figures 4-3a and 4-3b show a special mesh refinement that was done to fit the boundary layer near the airfoil wall.

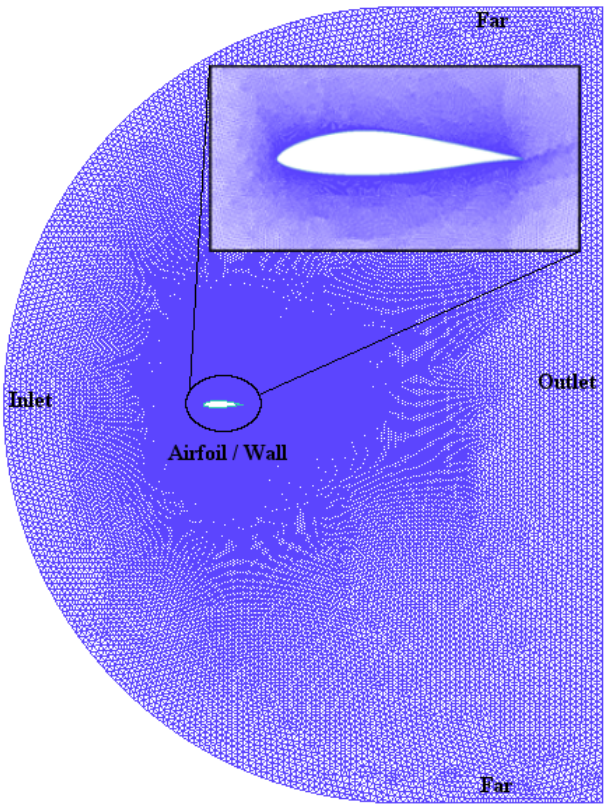

Figure 4-2: The constructed mesh around DU96-W-180 airfoil with the boundary conditions patches.

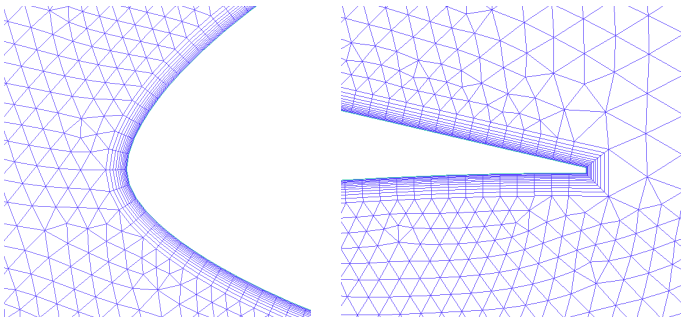

(a) The leading edge mesh. (b) The trailing edge mesh.

Figure 4-3: A closer view on the mesh cells around DU-96-W-180 airfoil.

The boundary conditions of the problem are defined along 5 patches as shown in Fig. 4-2. The pressure is *zeroGradient* everywhere except for the outlet where

its value is known to be atmospheric pressure. However, for the velocity, it's *fixedValue* and equal to the uniform *freestream* value at the inlet and the far boundaries, calculated for the outlet while for the wall boundary, it reduces to zero (due to no-slip condition). The chosen solver is *pisoFoam* which is used to solve incompressible unsteady flow by a PISO algorithm with a generic turbulence model option. For this problem case with low Re, the turbulence model is turned off to solve for laminar flow only. To ensure convergence, a sensitivity study was carried on. Three different probe locations (#3 near the separation bubble, #2 near the shear layer, and #1 in the wake region) were chosen in the computational domain for this study as plotted in Fig. 4-4.

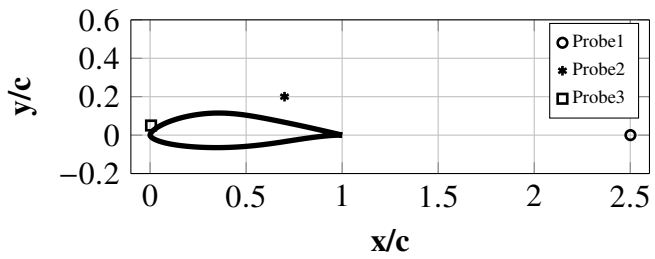

Figure 4-4: The probes locations used for the sensitivity study.

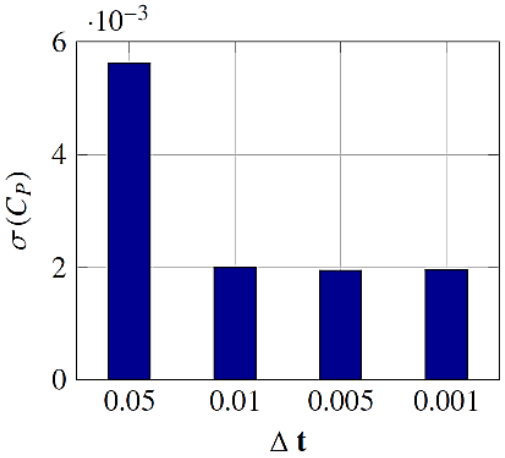

Figure 4-5: Pressure coefficient standard deviation at different time steps.

Different time resolutions were tested for those probes. From Figures 4-5 and 4-6, it is clear that standard deviation values for both C_p and U are relatively small for all probes. Thus using 0.05 s time step will be efficient and yield time independent solution with acceptable error.

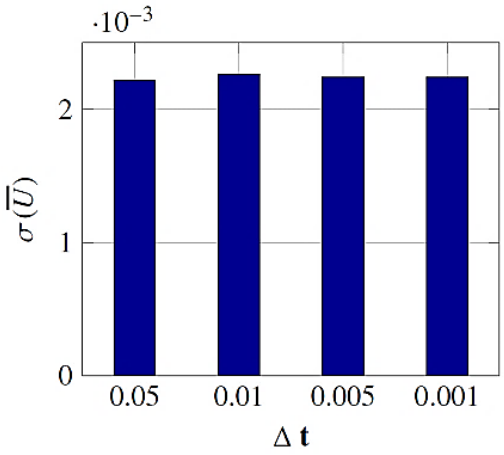

Figure 4-6: Normalized velocity standard deviation at different time steps.

Furthermore, since the mesh used in this thesis is much denser than the one used by Soltan,[45] and comparable to Elhadidi et al.,[46] so a grid independence is guaranteed for this study.

4.5 Fast Fourier Transform

As previously reviewed in Section 1.5.3, the boundary layer control can significantly improve the aerodynamic performance over the surface. Controlling and modifying the inherent instabilities in the boundary layer is a very effective means of flow control, and one way to achieve this is through periodic excitation [81–83].

According to the study done by Raju et al. [84], three distinctive locations have the most dominant frequencies affecting the vortical structures in the flow, the

separation wake, the shear layer, and the separation bubble regions. Thus, in order to achieve an optimum frequency for the flow control application, FFT analysis is required for these three locations. As shown in Figure 4-7, three probe locations were chosen to match the three distinctive locations that were under investigation. The probe locations have coordinates as follows:

Probe #1 (Wake region): $(x_1, y_1) = (17.537, 2.557)$

Probe #2 (Shear Layer region): $(x_2, y_2) = (4.115, 2.055)$

Probe #3 (Separation Bubble region): $(x_3, y_3) = (0.894, 0.744)$

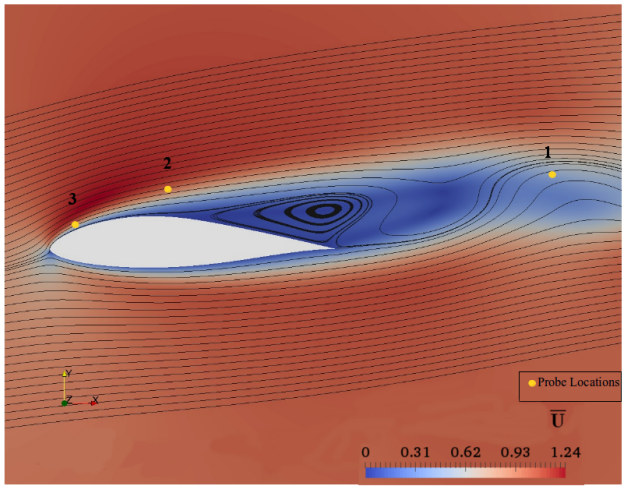

Figure 4-7: The three probe locations used to study FFT.

These probe locations data were extracted and then an FFT routine was constructed and applied using 20 Hz sampling frequency to the normalized cross-stream velocity, $\bar{U_y}$, variation as shown in Figures 4-8a to 4-8c where,

$$\overline{U_y} = \frac{U_y}{U_\infty} \tag{4.3}$$

From the shown FFT results, in Figure 4-8c the dominant frequency was found to be $\bar{f} = 0.68$ and obviously appears in the wake region which possess the most flow perturbations (energy) where,

$$\bar{f} = \frac{f \times c}{U_\infty} \tag{4.4}$$

In addition, the frequency value in the other regions of the mixing shear layer as in Fig. 4-8b, and the separation bubble as in Fig. 4-8a is so small (near zero) indicating very small vortical structures at these regions and thus insignificant impact on the overall domain dominant frequencies. Hence, actuating using the previously obtained dominant frequency should yield a better aerodynamic response and would save much time in trial and error tests in the active control phase as discussed in the following section.

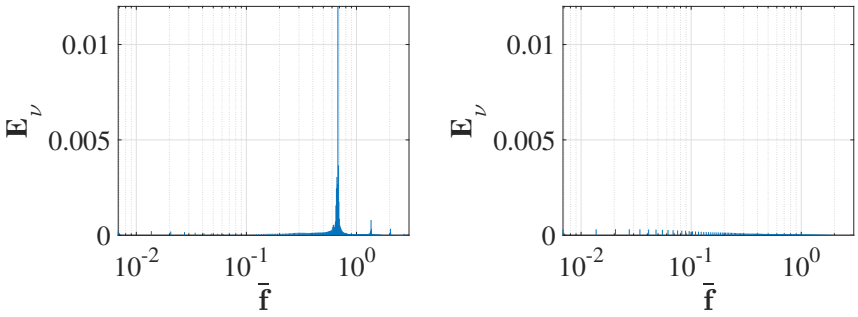

(a) Probe #1 FFT.

(b) Probe #2 FFT.

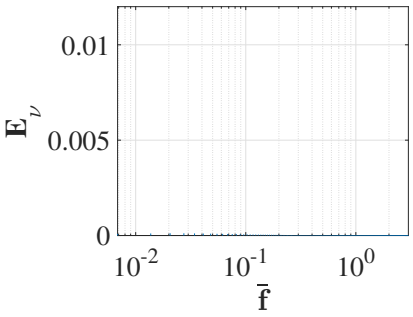

(c) Probe #3 FFT.

Figure 4-8: Cross-stream velocity FFT power spectra of 3 probe locations.

4.6 Flow Control Solver

In this work, periodic excitation is achieved efficiently (lowest energy addition/requirement) though a slat near the airfoil leading edge that periodically allow for the passing (blowing) of air from below the lower surface of the airfoil to its upper surface inertially.

A new solver was developed from the existing pisoFoam solver(See Appendix C.2 for more solver details). That solver was able to periodically excite the flow on the upper surface of the airfoil. That was achieved through modifying the pressure equation by adding a source term. To numerically simulate the effect of periodic opening and closing of the slat, a Darcy-Forcheimer porosity model was applied in the source term as in Equation 4.5.

$$\boldsymbol{S = |sin2\pi.fruntime|.DarcyForchheimerPorosityModel} \quad (4.5)$$

where, t is the simulation runtime,
f is chosen from various frequencies including the dominant frequency resulted from FFT analysis performed in section 4.5,
and DarcyForchModelCoeff [63] are the coefficients of the of the porosity model in the solver library defined as prescribed in OpenFOAM's fvOptions by Halawa [85, 86].

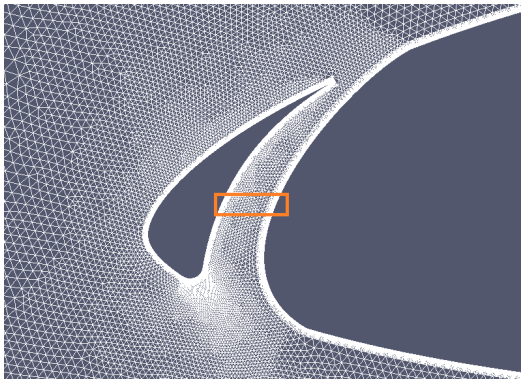

Figure 4-9: Slat mesh and the cells responsible for AFC.

The main objective of this model is to change the density of a bulk of cells spanning the passage of the slat as shown in Figure 4-9 (the cells enclosed by the orange rectangle). The density varies periodically (as a function of the running time) from a very high value (simulating a fully closed slat) back to the air density (simulating a fully open slat).

4.7 Uncontrolled Flow

In this section, simulations for both clean configuration airfoil and slatted airfoil will be shown. The computations were carried on till $\bar{t} = 47.45$ (130,000 time-step of 0.05 s) where $\bar{t}$ is non-dimensional time parameter defined as,

$$\bar{t} = \frac{\bar{t} \times U_\infty}{c} \tag{4.6}$$

where U_∞ is the free stream velocity and c is the chord length.

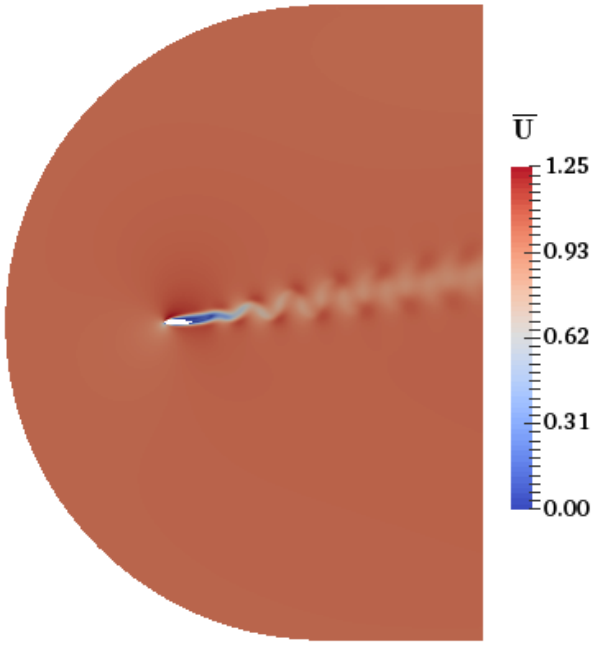

Figure 4-10: Velocity distribution around the airfoil at $\bar{t} = 47.45$ showing the unsteady Kármán vortex shedding.

Firstly, the unslatted (clean configuration) airfoil case was simulated. The normalized velocity distribution for the computational domain is presented in Figure 4-10 where the unsteady Kármán vortex shedding is obvious after the trailing edge of the airfoil.

Next, the flow field is simulated for the case of uncontrolled slat. The results shown in Figures 4-11 and 4-12 are for the velocity contours for the open slat case, where the source term is zero, and the closed slat case (exactly resembles the clean airfoil case), where the source term is nonzero and controlled by the Darcy Forchheimer Porosity Model in the OpenFOAM library, respectively.

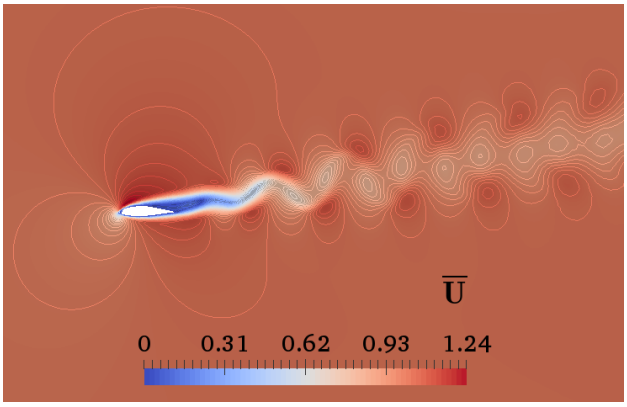

Figure 4-11: Velocity contours for the flow around the "open-slat" DU96-W-180 airfoil.

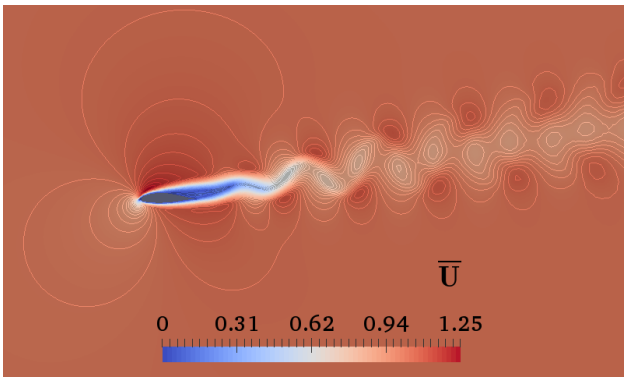

Figure 4-12: Velocity contours for the flow around the "closed-slat" DU96-W-180 airfoil.

It is worthy to note that as shown from Figures 4-11 and 4-12, both the open and closed slat simulations showed similar trailing edge shedding, thus any application of reduced order modelling (ROM) as the Proper Orthogonal Decomposition (POD) or Modified Linear Stochastic Measurement (MLSM) methods on either of them is acceptable [85, 86] as verified with El-desouky's work too [87]. Furthermore, Figures 4-13 and 4-14 show a close-up view for velocity and pressure contours of the case of the closed-slatted airfoil simulations, respectively. That is clearly showing the effect of the slat blockage on the velocity that is reduced to zero inside the slat that resembles the case of no-slat airfoil (clean configuration).

On top of that, the accumulation of the flow in the lower portion of the slat led to a high-pressure zone as shown.

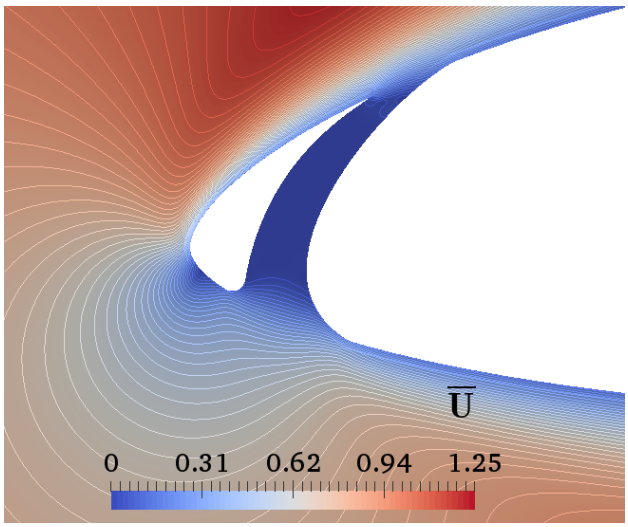

Figure 4-13: Pressure coefficient contours for the flow around the "closed-slat" DU96-W-180 airfoil.

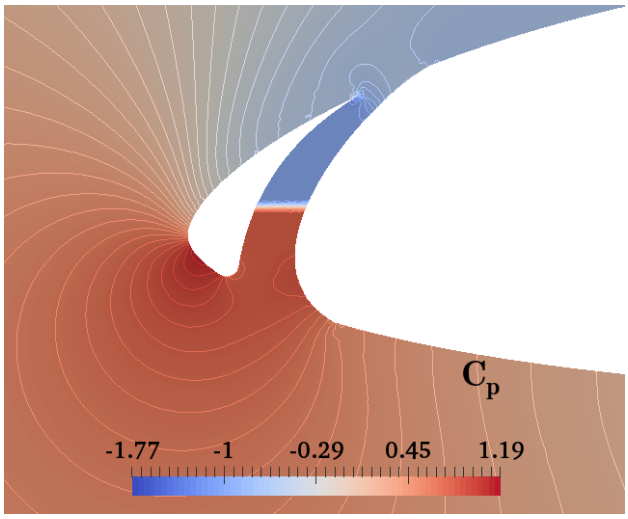

Figure 4-14: Normalized velocity contours for the flow around the "closed-slat" DU96-W-180 airfoil.

Moreover, a noticeable improvement in the aerodynamic properties was achieved

due to the open slat as shown in the Figures 4-15 and 4-16. The lift coefficient was boosted by around 8% of its value when the slat was closed (clean configuration/ no-slat case). Furthermore, an improvement in aerodynamic efficiency was achieved by about 3.1%.

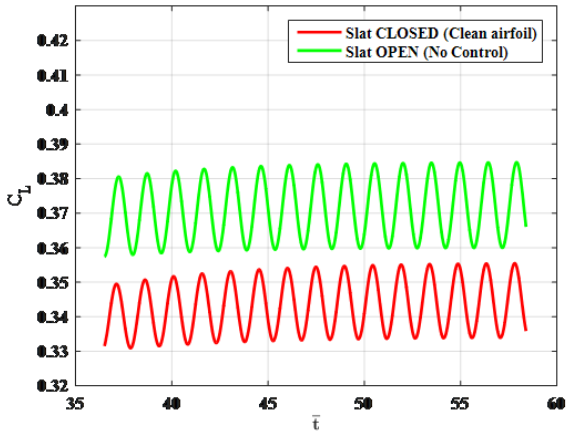

Figure 4-15: Temporal variation of the Lift coefficient for both clean and active slat.

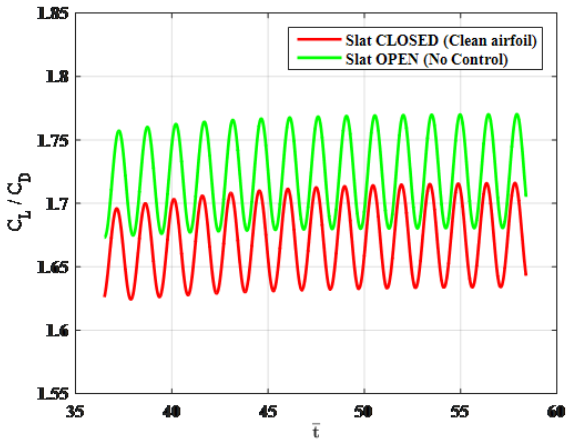

Figure 4-16: Temporal variation of the Aerodynamic efficiency for both clean and active slat.

4.8 Active Flow Control

Table 4.2: A quantitative summary of the open-loop periodic slat simulations results.

#	Simulation	Normalized Frequency ($\bar{f}$)	Control Start Time ($\bar{t}$)	ΔC_L %	$\Delta \frac{C_L}{C_D}$ %
1	Clean/ Closed Slat	–	–	0.0000	0.0000
2	No Control/ Open Slat	–	–	7.9937	3.1030
3	AFC	0.68	00.00	4.8853	1.8851
4	AFC	0.68	36.50	6.8479	2.6530
5	AFC	6.85	00.00	-0.5013	-0.2188
6	AFC	6.85	08.76	1.3494	0.5266
7	AFC	6.85	43.50	5.8128	2.1859
8	AFC	13.69	00.00	-1.0894	-0.1206
9	AFC	13.69	43.50	5.5926	2.1416
10	AFC	136.99	36.50	5.4335	2.4385

For open-loop control, the flow was controlled by a periodic slat (Open/Closed) that was simulated using the porosity model described earlier in Section 4.6. Several AFC simulations were carried out for different parameters. One of which is the excitation frequency, where f, in Equation 4.5 is substituted by the dominant frequencies obtained from FFT analysis in section [85], alongside testing other values in order to obtain the most convenient one. The other variable is time, where the different excitation initiation times had been tested. AFC was tested at different times t, in Equation 4.5 such as at the start of simulation ($\bar{t} = 0$), at

a transient time ($\bar{t} = 8.76$), and at a complete shedding (wake formation) time ($\bar{t} = 43.50$). A summary of these trials is tabulated in Table 4.2.

The shown results in Figure 4-17 and 4-18 are samples from the results in Table 4.2, namely case #4 which has the best improvements in the lift coefficient, drag coefficient, and the aerodynamic efficiency distribution at the dominant domain frequency .

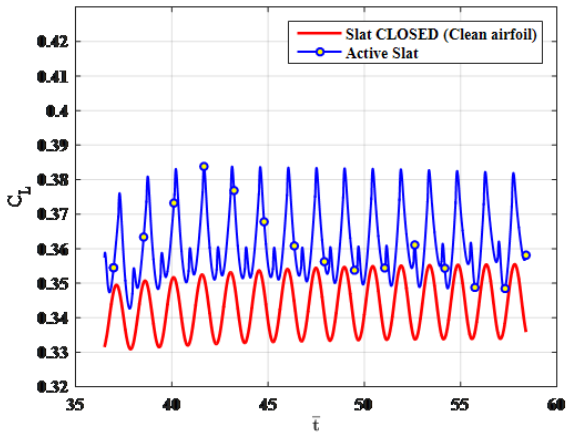

Figure 4-17: Temporal variation of the Lift coefficient for both clean and active slat with periodic porosity $\bar{f} = 0.68$.

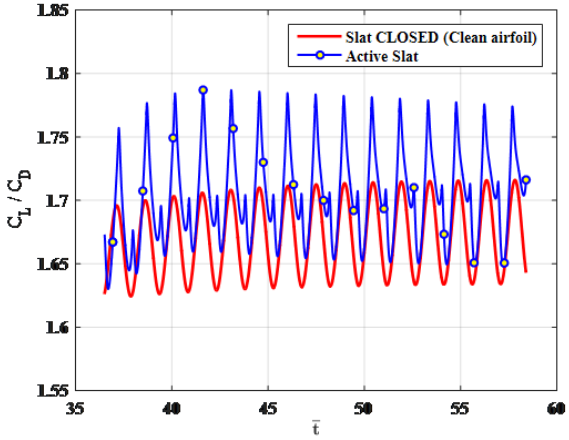

Figure 4-18: Temporal variation of the aerodynamic efficiency for both clean and active slat with periodic porosity $\bar{f} = 0.68$.

Additionally, Figure 4-19 shows the achievement in the lift coefficient with respect to the input frequency.

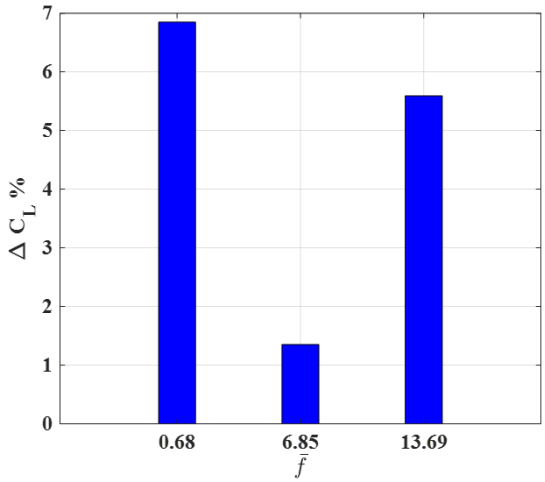

Figure 4-19: Averaged lift coefficient percentage increase by AFC.

From the previous results, it is clear that starting the active slat excitation (control) after the full wake (shedding) is formed showed better aerodynamic efficiency for all tested frequencies rather than starting the excitation from the beginning of the simulation. Thus, this will save much computational time and cost. As expected from the FFT analysis [85], the dominant frequency showed the best results among other active control results. Likewise, the recent results obtained by Elhadidi et al. [46]), the open-loop (uncontrolled) slat shows best results among all open-loop trials near the same angle of attack. Consequently, closed-loop implementation within OpenFOAM's solver is essential as a next step for achieving better aerodynamic performance.

4.9 Summary

In this chapter the active flow control technique was presented to investigate its influence on the improvement of the airfoil aerodynamic properties. Various numerical simulations (uncontrolled and controlled) were done for an incompressible, unsteady air flow over a DU-96-W-180 airfoil using a newly developed OpenFOAM solver. Different actuation frequencies were tested to get the optimum actuation frequency value. It was clear that using the active slat resulted in an accelerated downstream flow, hence, increased mixing and improved performance of the airfoil. Furthermore, using FFT analysis had contributed well in the flow control analysis by narrowing the values of the actuation frequency. It showed the most dominant frequencies to be used in the active flow control actuation. FFT saved much computational time that would be wasted on testing a wide range of values. Operating the active slat at this dominant frequency yielded the best performance enhancement. That enhanced performance was reflected as an improvement in the lift coefficient up to 8% and in the overall aerodynamic efficiency by 3% compared to the clean airfoil configuration.

Chapter 5

Conclusion

The aim of the project was to produce a review and to get a better understanding of wind turbine blades aerodynamics, by means of a wide-range CFD simulations. Several issues were addressed, mainly the stall phenomena and the flow control technique as well as the fluid-structure interaction (aeroelastic) effects on the wind turbine blades. The results from the computations were quite satisfactory and, in our opinion, they can represent a good foundation for future work in this area. The more significant findings are summarized below.

In Chapter 3, for the precomputational aerodynamic study, the stall performance was successfully captured numerically and validated by the experimental data with a reasonable error. Besides, it was obvious the k–ω SST turbulence model was an effective choice to appropriately capture this case physical behavior up to the stall. However, further simulations are required by using more sophisticated turbulence simulations like the Improved Delayed Detached Eddy Simulation (IDDES) as well as transitional models which needs huge amount of resources. The post-stall characteristics and the stall dynamic behavior would be one of the future applications of this work. In addition the extension of this work to three-dimensional applications like a whole wind turbine blade is an important

development.

On the other hand, using the previous turbulence model and mesh sizing recommendations, FSI simulations were held on the full-scale rotor blades of the NREL 5MW reference HAWT. The results were validated against the various FSI codes like the BEM-based FAST and FLEX5-Q^{3}UIC as well as the vortex-method based MIRAS-FLEX. The results from all codes were generally in a very good agreement for both the aerodynamic and structural parts. The results match well near the rated wind speed while slightly vary beyond it due to the inherent instabilities associated with higher wind speeds that needs further study. The differences are also due to the 2D assumptions in the airfoil models in the FSI codes as well as the simplified inertial and gravitational effects in the CFD method. The current simulations shows a good prediction for the FSI behavior of the NREL 5MW HAWT rotor which will help developing more complicated solvers in the future.

One aspect to account for in the coming work also, is to perform FSI analysis using more complex inlet flow conditions to aid in studying the different instabilities in the flow. Besides, the FSI technique should be upgraded to the more realistic transient 2-way approach to achieve better accuracy and prediction of the turbine behavior and response to the various flow stimulants. Additionally, the studies will be upgraded to cover the unsteady dynamic behavior of the flow around the turbine in both the stall and FSI studies. Last but not the least, further simulations on the NREL 5MW turbine model are being carried out on another in-house developed Open-Source solver and will be published soon.

In Chapter 4, the CFD simulations were used to investigate the influence of active flow control on the improvement of the airfoil aerodynamic properties. Thus, better aerodynamic efficiency, delayed separation, reduced drag force, and

less unsteady fluctuations. To achieve this, a flow simulation around both clean and slatted configurations of a DU96-W-180 airfoil was done using OpenFOAM. Frequency analysis was done using FFT to three distinctive domain points to get the dominant frequencies. Finally, active flow control was applied using a novel active slat operating at the dominant frequencies obtained earlier to excite the flow leading to better flow attachments and aerodynamic properties.

- The use of the slat resulted in an accelerated downstream flow, hence, increased mixing and improved performance of the airfoil.

- Frequency analysis techniques, namely FFT, had contributed well in the flow control analysis by narrowing the values of the actuation frequency. It showed the most dominant frequencies to be used in the active flow control actuation. Its value was found to be $\bar{f} = 0.68$ and is located in the wake region. The reason behind this is that the downstream vortex shedding had high frequency and disturbed flow than upstream locations. Thus, FFT saved much computational time that would be wasted on testing a wide range of values.

- Obviously, slatting the airfoil and allowing a fresh (accelerated) boundary layer to add extra momentum to the flow improves the mixing and consequently the performance of the airfoil. An improvement in the lift coefficient was achieved of up to 8% and in the overall aerodynamic efficiency by 3% compared to the clean airfoil configuration. However, compared to the slatted uncontrolled case, the improvement was not enough promising, thus imposing a high necessity to apply closed-loop control to get better desired results.

- Active flow control simulations were applied using different actuation frequencies. It was deduced, as expected, that the dominant frequency showed

the best results among all other open-loop results. The lift enhancements were up to 7% in the lift coefficient and 3% in the overall aerodynamic efficiency compared to the clean airfoil configuration.

- OpenFOAM CFD toolbox shows great reliability and flexibility in simulations where any edits and developments could be easily done to the source code. Besides, the open parallelism feature provides great productivity.

For future work, it is recommended to investigate various slat locations to determine optimum location. Besides, applying closed loop (feedback) control is necessary to get optimized control action and yield better aerodynamic results on the airfoil. Increasing Re and solving for the turbulent flow need to be investigated. In addition, different angles of attacks should be studied to lock to the most critical and responsive one. Additionally, extension of this work to 3D simulations will be effective in matching practical wing cases. Furthermore, this work could be extended beyond fixed wing applications to include rotary blades. One of the promising applications is active control of the blade flutter of wind turbines using aerodynamic control [85, 86].

Bibliography

[1] Cosmos Magazine, URL: https://cosmosmagazine.com/climate/where-does-wind-come/ Accessed: 2018.

[2] General Electric Ltd., URL: https://www.ge.com/renewableenergy/wind-energy/ technology/ what-is- wind-energy/ Accessed: 2018.

[3] Argonne National Laboratory, Wind Energy Department, URL: http://windeis.anl.gov/guide/basics/ Accessed: 2018.

[4] Wind Energy Foundation, URL: http://windenergyfoundation.org/about-wind-energy/history/ Accessed: 2018.

[5] Cutler J 2004 History of Wind Energy - Encyclopedia of Energy *Boston: Elsevier* **6**.

[6] Ivanell S S A 2009 Numerical Computations of Wind Turbine Wakes *PhD Dissertation* KTH Mechanics Royal Institute of Technology Stockholm Sweden.

[7] LM Wind Power, URL: https://www.lmwindpower.com/en/sustainability/learn-about-wind /history-of-wind Accessed: 2018.

[8] Dutch windmills, URL: https://en.wikipedia.org/wiki/Windmill Accessed: 2018.

[9] U.S. Energy Information Administration, URL: https://www.eia.gov/energyexplained/index.php?page=wind _history Accessed: 2018.

[10] Vestas, Offshore V164-8.0 MW, V112-3.3 MW, URL: http://www.vestas.com/en/wind-power-plants/procurement/turbine-overview/v164-8.0-mw -offshore.aspx Accessed: 2018.

[11] Bak C, Zahle F, Bitsche R, Kim T, Yde A, Henriksen L C, Hansen M H, Blasques J P A A, Gaunaa M and Natarajan A 2013 The DTU 10-MW Reference Wind Turbine *Danish Wind Power Research* Fredericia Denmark.

[12] Linul E and Marsavina L 2013 Mechanical Characterization of Rigid PUR Foams Used for Wind Turbine Blades Construction *In Recent Advances in Composite Materials for Wind Turbines Blades; WAP-AMSA* .

[13] Annual OEM research by BTM Navigant, URL: https://www.windpowermonthly.com/article/1340513/vestas-stays-number-one-btm-navigant-survey Accessed: 2018.

[14] Ivanell S, Sørensen J N, and Henningson D 2007 Numerical Computations of Wind Turbine Wakes *Wind Energy* Springer Berlin Heidelberg 259-263.

[15] Global Wind Energy Council Report 2017, URL: http://gwec.net/global-figures/graphs/ Accessed: 2018.

[16] Carcangiu C E 2008 CFD-RANS study of horizontal axis wind turbines *PhD thesis* Universita'degli Studi di Cagliari.

[17] Hsu M C, Bazilevs Y 2012 Fluid–structure interaction modeling of wind turbines: simulating the full machine *Computational Mechanics* **50** 6 821-833.

[18] Rafiee R, Tahani M, and Moradi M 2016 Simulation of aeroelastic behavior in a composite wind turbine blade *Journal of Wind Engineering and Industrial Aerodynamics* **151** Supplement C 60-69.

[19] Wang L, Quant R, and Kolios A 2016 Fluid structure interaction modelling of horizontal-axis wind turbine blades based on CFD and FEA *Journal of Wind Engineering and Industrial Aerodynamics* **158** Supplement C 11-25.

[20] Carrión M, Steijl R, Woodgate M, Barakos GN, Munduate X, and Gomez-Iradi S 2014 Aeroelastic analysis of wind turbines using a tightly coupled CFD-CSD method *Journal of Fluids and Structures* **50** Supplement C 392-415.

[21] Heinz J C, Sørensen N N, Zahle F and Skrzypiński W R 2016 Vortex-induced vibrations on a modern wind turbine blade *Wind Energy* **19** 2041-2051.

[22] Heinz J C, Sørensen N N and Zahle F 2016 Fluid-structure interaction computations for geometrically resolved rotor simulations using CFD *Wind Energy* **19** 2205-2221.

[23] Dose B, Rahimi H, Herráez I, Stoevesandt B and Peinke J 2016 Fluid-structure coupled computations of the NREL 5MW wind turbine blade during standstill *Journal of Physics: Conference Series* **753** 2 022-034.

[24] Bazilevs Y, Hsu M C, Akkerman I, Wright S, Takizawa K, Henicke B, Spielman T and Tezduyar T E 2011 3D simulation of wind turbine rotors at full scale. Part I: Geometry modeling and aerodynamics *International Journal for Numerical Methods in Fluids* **65** 207-235.

[25] Sessarego M, Ramos García N, Sørensen J N and Shen WZ 2017 Development of an aeroelastic code based on three-dimensional viscous-inviscid method for wind turbine computations *Wind Energy* **20** 7 1145-1170.

[26] Øye S 1996 FLEX4 simulation of wind turbine dynamics *Proceedings of the 28th IEA Meeting of Experts Concerning State of the Art of Aeroelastic Codes for Wind Turbine Calculations* International Energy Agency Lyngby Denmark 71–76.

[27] Jonkman J M and Buhl Jr M L 2005 FAST User's Guide *Technical Report* NREL/EL-500-29798 National Renewable Energy Laboratory Golden Colorado United States.

[28] Jahanmiri M 2010 Active Flow Control: A Review *Research Report* Chalmers University of Technology Göteborg **12**.

[29] Gross A and Fasel H F 2008 CFD for Investigating Active Flow Control *AIAA 4th Flow Control Conference* Seattle Washington.

[30] Miller D N and Joslin R D 2009 Fundamentals and Applications of Modern Flow Control *AIAA* Reston VA.

[31] Collis S S, Joslin R D, Seifert A and Theofilis V 2004 Issues in active flow control: theory, control, simulation, and experiment, *Progress in Aerospace Sciences* **40** Elsevier May-July pp. 237-289.

[32] Jirásek A 2005 Vortex-Generator Model and Its Application to Flow Control *JOURNAL OF AIRCRAFT, November - December* **42** 6.

[33] Yamouni S, Mettot C, Sipp D and Jacquin L 2013 Passive Control of Cavity Flows *Aerospace Lab* **6**.

[34] Williams D R and MacMynowski D G 2009 Brief History of Flow Control *Progress in Astronautics and Aeronautics, AIAA* Fundamentals and Applications of Modern Flow Control 1-20.

[35] Barlas K T and Kuik G V 2010 Review of state of the art in smart rotor control research for wind turbines *Progress in Aerospace Sciences* **46** 1 pp. 1-27.

[36] Cattafesta L N I, Garg S and Shukla D 2001 The Development of Piezoelectric Actuators for Active Flow Control *AIAA Journal* **39** 8 pp. 1562-1568.

[37] Mathew J, Song Q, Sankar B V, Sheplak M and Cattafesta L N 2006 Optimized Design of Piezoelectric Flap Actuators for Active Flow Control, *AIAA Journal* **44** 12 pp. 2919-2928.

[38] Dialoupis A 2014 Active Flow Control Using Plasma Actuators Application on Wind Turbines *Master's thesis* Delft University of Technology.

[39] Glezer A and Amitay M 2002 Synthetic Jets *Annual Review of Fluid Mechanics* **34** pp. 503-529.

[40] Raju R, Mittal R, Gallas Q and Cattafesta L 2005 Scaling of Vorticity Flux and Entrance Length Effects in Zero-Net Mass-Flux Devices, *35th AIAA Fluid Dynamics Conference and Exhibit*.

[41] Cattafesta L N and Sheplak M 2011 Actuators for Active Flow Control *Annual Review of Fluid Mechanics* **43** 1 247-272.

[42] Moreau E 2007 Airflow Control by Non-Thermal Plasma Actuators *Journal of Physics D: Applied Physics* **40** pp. 605-636.

[43] Corke T C, Enloe C L and Wilkinson S P 2010 Dielectric barrier discharge plasma actuators for flow control *Annu. Rev. Fluid Mech.* **42** 505-29.

[44] Smith A M O 1975 High-lift aerodynamics *Journal of Aircraft* **12** 6 pp. 501-530.

[45] Soltan T M 2015 Application of Active Slat to Control Flow over a NACA 4418 airfoil at Re=40,000 *Master's thesis* Cairo University.

[46] Elhadidi B, Elqatary I, Mohamady O and Othman H 2015 Experimental and Numerical Investigation of Flow Control Using a Novel Active Slat *International Journal of Mechanical, Aerospace, Industrial, Mechatronic and Manufacturing Engineering* **9** 1 pp. 21-25.

[47] Sørensen J N and Shen W Z 2002 Numerical modeling of wind turbine wakes *Journal of Fluid Engineering* **124** 393-9.

[48] Sørensen J N 2010 Aerodynamics aspects of wind energy conversion *Annual Review of Fluid Mechanics* **43** 427-448.

[49] Tossas L A M and Leonardi S 2013 Wind turbine modeling for computational fluid dynamics: December 2010-December 2012 *Technical Report* NREL/SR-5000-55054 National Renewable Energy Laboratory Golden Colorado United States.

[50] Burton T, Sharpe D, Jenkins N and Bossanyi E 2002 Aerodynamics of Horizontal-Axis Wind Turbines *John Wiley & Sons, Ltd* 41-172.

[51] Manwell J F, McGowan J G, and Rogers A L 2010 Wind Energy Explained: Theory, Design and Application *John Wiley & Sons, Ltd*.

[52] Sanderse B, Van der Pijl S P, and Koren B 2011 Review of computational fluid dynamics for wind turbine wake aerodynamics *Wind Energy* **14**.

[53] Vermeer L J, Sørensen J N and Crespo A 2003 Wind turbine wake aerodynamics *Progress in Aerospace Sciences* **39** 467-510.

[54] Hansen M O L, Sørensen J N, Voutsinas S, Sørensen N, and Madsen H A 2006 State of the art in wind turbine aerodynamics and aeroelasticity *Progress in Aerospace Sciences* **42** 285-330.

[55] Benjanirat S, Sankar L N and Xu G 2003 Evaluation of turbulence models for the prediction of wind turbine aerodynamics *In Proc. of 41st AIAA Aerospace Sciences Meeting and Exhibit* **517**.

[56] Simscale, URL: https://www.simscale.com/docs/content/simulation/model/turbulenceModel/kOmegaSST.html Accessed: 2018.

[57] CFD-Online, URL: https://www.cfd-online.com/Wiki/Turbulence _free-stream _boundary _conditions Accessed: 2018.

[58] Menter F R 1992 Improved Two-Equation k-omega Turbulence Models for Aerodynamic Flows *Technical Report* NASA TM 103975 National Aeronautics and Space Administration NASA Ames Research Center Moffett Field CA United States.

[59] Menter F R 1993 Zonal Two Equation k-omega Turbulence Models for Aerodynamic Flows *AIAA Journal* pp. 93-2906.

[60] Menter F R 1994 Two-Equation Eddy-Viscosity Turbulence Models for Engineering Applications *AIAA Journal* **32** 8 pp. 1598-1605.

[61] VV.AA. Fluent 18 Documentation, user's guide. Technical report, ANSYS Inc., 2017.

[62] Fluent 18 Documentation, theory guide. Technical report, ANSYS Inc., 2017.

[63] OpenFOAM® Programmer's Guide Official Website: https://www.openfoam.org/ Accessed: 2017.

[64] Versteeg H K and Malalasakera W 1995 An Introduction to Computational Fluid Dynamics: The Finite-Volume Method *Harlow : Longman Scientific & Technical* New York.

[65] Ferziger J H and Peric M 1999 Computational Methods for Fluid Dynamics *Springer-Verlag* Berlin.

[66] Kang S and Hirsch C 2001 Features of the 3D flow around wind turbine blades based on numerical solutions *In Proceedings of EWEC* **06** Copenhagen.

[67] Mikkelsen R 2003 Actuator disc methods applied to wind turbines *PhD Dissertation* Technical University of Denmark.

[68] Alinot C and Masson C 2002 Aerodynamic simulation of wind turbines operating in atmospheric boundary layer with various thermal stratifications *In Proc. of 40th AIAA Aerospace Sciences Meeting and Exhibit* 1-10.

[69] Xu G and Sankar L N 1999 Computational study of HAWT *In Proc. of 37th AIAA Aerospace Sciences Meeting and Exhibit* **48**.

[70] Xu G and Sankar L N 2000 Effects of transition, turbulence and yaw on the performance of hawt *In Proc. of 38th AIAA Aerospace Sciences Meeting and Exhibit* **48**.

[71] Benjanirat S and Sankar L N 2004 Recent improvements to a combined Navier-Stokes full potential methodology for modeling HAWTs *In Proc. of 42nd AIAA Aerospace Sciences Meeting and Exhibit* **830**.

[72] Ramos G N, Sørensen J N and Shen W Z 2014 A strong viscous–inviscid interaction model for rotating airfoils *Wind Energy* **17** 12 pp. 1095-4244.

[73] Ramos G N, Hejlesen M M, Sørensen J N and Walther J H 2017 Hybrid vortex simulations of wind turbines using a three-dimensional viscous–inviscid panel method *Wind Energy* **20** 11 pp. 1871-1889.

[74] Oracle Corporation. Oracle Solaris Studio, 500 Oracle Parkway, Redwood Shores, CA 94065. http://www.oracle.com.

[75] Øye S 1991 Dynamic stall, simulated as a time lag of separation *4th IEA Symposium on the Aerodynamics of Wind Turbines* McAnulty KF (ed.) ETSU-N-118: Harwell Laboratory Harwell UK.

[76] Schepers JG and Snel H 1995 Dynamic inflow: yawed conditions and partial span pitch control *Netherlands Energy Research Foundation* Technical Report ECNC-95-056 Petten The Netherlands.

[77] Snel H and Schepers JG 1995 Joint investigation of dynamic inflow effects and implementation of an engineering method *Netherlands Energy Research Foundation* Technical Report ECNC-94-107 Petten The Netherlands.

[78] Boorsma K and Schepers J G 2016 Rotor experiments in controlled conditions continued: New Mexico *Journal of Physics: Conference Series* **753** 022004.

[79] Jonkman J M, Butterfield S, Musial W and Scott G 2009 Definition of a 5-MW Reference Wind Turbine for Offshore System Development *Technical Report* NREL/TP-500-38060 National Renewable Energy Laboratory Golden Colorado.

[80] Phelps C and Singleton J 2011 Wind Turbine Blade Design *Technical Report* Cornell University.

[81] Hsiao F, Liu C F and Shyu J Y 1990 Control of Wall-Separated Flow by Internal Acoustic Excitation *AIAA Journal* **28** 8 pp. 1440-1446.

[82] Seifert A, Darabi A and Wygnanski I 1996 Delay of Airfoil Stall by Periodic Excitation *Journal of Aircraft* **33** 4 pp. 691-698.

[83] Zaman, K. and Bar-Sever, A. and Mangalam, S. 1987 Effect of Acoustic Excitation on the Flow Over an Low-Re Airfoil *Journal of Fluid Mechanics* **182** pp. 127-148.

[84] Raju, R., and Mittal, R. 2008 Dynamics of Airfoil Separation Control Using Zero-Net Mass-Flux Forcing *AIAA Journal* **46** 12 pp. 3103-3115.

[85] Halawa A M, Elhadidi B, and Yoshida S 2018 Aerodynamic Performance Enhancement Using Active Flow Control on DU96-W-180 Wind Turbine Airfoil *Evergreen Journal* **5** 1 pp. 16-24.

[86] Halawa A M, Elhadidi B, and Yoshida S 2017 POD & MLSM Application on DU96-W180 Wind Turbine Airfoil *Evergreen Journal* **4** 1 pp. 36-43.

[87] El-Desouky M I 2009 Flow Control For Circular Cylinder Using Proper Orthogonal Decomposition *Master Thesis* Cairo University.

[88] OpenFOAM® User's Guide Official Website: https://www.openfoam.org/ Accessed: 2016.

[89] Website: https://sourceforge.net/projects/foam-extend/ Accessed: 2017.

[90] Hua-Dong Y 2014 Simulation of Fluid-Structural Interaction using OpenFOAM *Report* Department of Applied Mechanics Chalmers University of Technology.

[91] Timmer W A 2010 Aerodynamic characteristics of wind turbine blade airfoils at high angles-of-attack *TORQUE 2010: The Science of Making Torque from Wind* June 28-30 Crete Greece.

[92] Halawa A M 2016 Active Flow Control for DU96-W-180 Airfoil at Low Reynolds Number by an "Active Slat" *APISAT 2016: Asia-Pacific International Symposium on Aerospace Technology* October 25-27 Toyama Japan.

[93] Heinz J C, Sørensen N N and Zahle F 2013 Partitioned fluid–structure interaction for full rotor computations using CFD *PhD Thesis* Technical University of Denmark.

[94] Farhat C, Van der Zee K G and Geuzaine P 2006 Provably second-order time-accurate loosely-coupled solution algorithms for transient nonlinear computational aeroelasticity *Computer Methods in Applied Mechanics and Engineering* **195** pp. 1973–2001.

Appendices

Appendix A

Rotor Parameters

The chosen wind turbine for the study is the land-based version of the National Renewable Energy Laboratory (NREL) 5-MW offshore baseline wind turbine [79] with a rotor diameter of 126 m. Table A.1 summarizes the gross properties of the NREL 5-MW turbine.

Table A.1: Gross properties of the NREL 5-MW baseline wind turbine [79].

Rated power	5 MW
Rotor orientation, configuration	Upwind, 3 blades
Control	Variable speed, collective pitch
Drivetrain	High-speed, multiple-stage gearbox
Rotor, hub diameter	126 m, 3 m
Hub height	90 m
Cut-in, rated, cut-out wind speed	3 m/s, 11.4 m/s, 25 m/s
Cut-in, rated rotor speed	6.9 RPM, 12.1 RPM
Rated tip speed	80 m/s
Overhang, shaft tilt, precone	5 m, 5^o, 2.5^o
Rotor mass	110,000 kg
Nacelle mass	240,000 kg
Tower mass	347,460 kg

NREL, National Renewable Energy Laboratory.

The NREL 5-MW turbine consists of Delft University of Technology (DU) airfoils between 40% and 21% relative thickness and an 18% NACA airfoil in the blade tip region as shown in Figures A-1 and A-2.

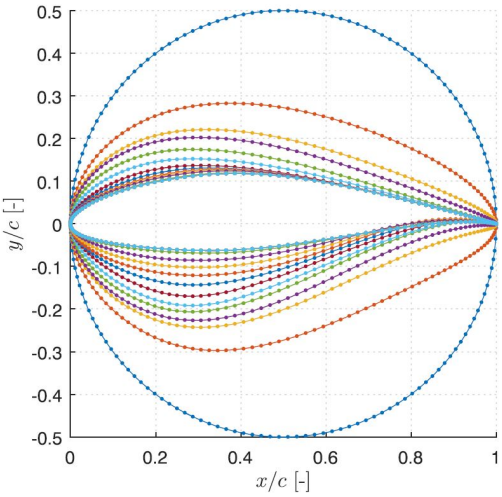

Figure A-1: NREL 5-MW blade cross-sectional profiles [25].

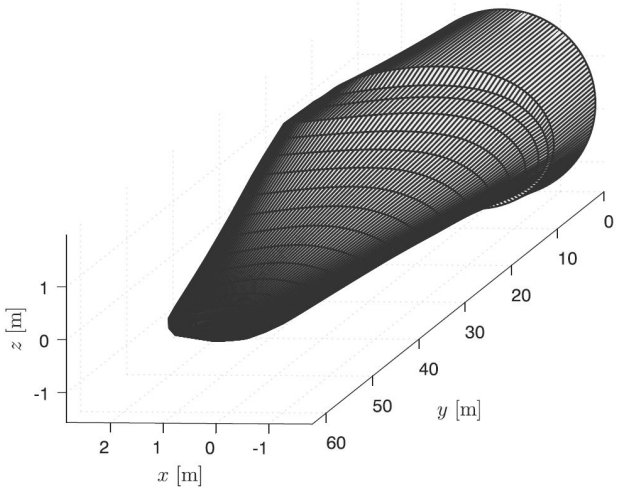

Figure A-2: NREL 5-MW blade mesh generated in MIRAS-FLEX with 20 stations in the span-wise direction [25].

Appendix B

Betz Limit

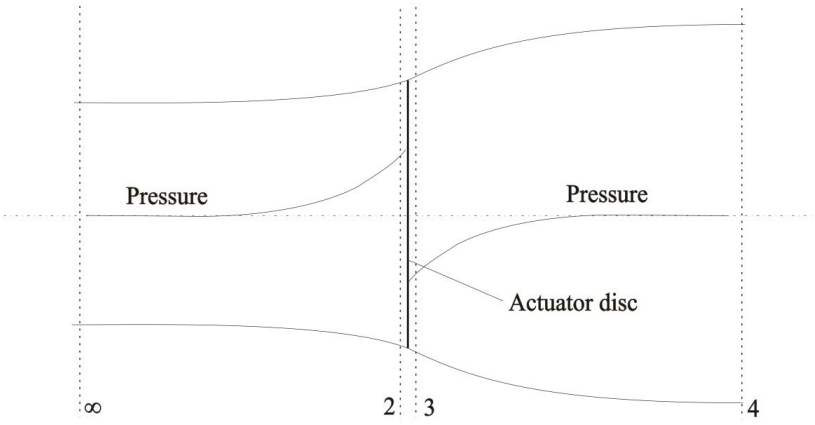

Figure B-1: The actuator disc concept [6].

For steady state flow $(\rho AU)_\infty = (\rho AU)_4 = \dot{m}$ where $\dot{m}$ is the mass flow rate and the index 4 notes the position according to Figure B-1. The thrust force is therefore equal to the mass flow multiplied with the change in velocity [6].

$$T = \dot{m}(U_\infty - U_4) \tag{B.1}$$

Applying requirements for continuity, momentum balance, and energy balance

to the flow, the thrust and power can be determined if the assumptions above are fulfilled.

Firstly, from the momentum theorem, the thrust is:

$$T = U_\infty(\rho AU)_\infty - U_4(\rho AU)_4 \tag{B.2}$$

where ρ is the air density, A the cross section area, U_∞ the free stream velocity and U_2, U_3, U_4 the velocities at different locations according to Figure B-1.

Secondly, from the pressure drop caused by the actuator disc, which represents the turbine, the thrust can also be derived by using the Bernoulli principle separately on each side of the turbine.

In the stream tube upstream of the disc:

$$p_\infty + \frac{1}{2}\rho U_\infty^2 = p_2 + \frac{1}{2}\rho U_2^2 \tag{B.3}$$

In the stream tube downstream of the disc:

$$p_3 + \frac{1}{2}\rho U_3^2 = p_4 + \frac{1}{2}\rho U_4^2 \tag{B.4}$$

Since two of the assumptions for this model are that $p_\infty = p_4$ and that the velocity across the disc remains the same ($U_2 = U_3$), the thrust can also be expressed as:

$$T = A(p_2 - p_3) \tag{B.5}$$

If one solves Equations B.3 and B.4 for $(p_2 - p_3)$ and substitutes that into B.5, one obtains:

$$T = \frac{1}{2}\rho A_2(U_\infty^2 - U_4^2) \tag{B.6}$$

Combining B.1 and B.6 gives:

$$\dot{m}(U_\infty - U_4) = \frac{1}{2}\rho A_2(U_\infty^2 - U_4^2) \tag{B.7}$$

Recognizing that $\dot{m} = \rho A_2 U_2$ or $\dot{m} = \rho A_3 U_3$ (index 2 will be used for the disc from now on), the result generally known as Froude's theorem is obtained.

$$U_2 = \frac{U_\infty + U_4}{2} \tag{B.8}$$

The interpretation of this expression is that the velocity at the disc is the average of the free stream and far wake velocities, so the total velocity change from free stream to far wake is twice the change from free stream to the disc.

Now introducing the axial interference factor which is a measure of the turbine influence to the wind (induced velocity) and defined as:

$$a = \frac{U_\infty - U_2}{U_\infty} \tag{B.9}$$

which gives:

$$U_2 = U_\infty(1 - a) \tag{B.10}$$

$$U_4 = U_\infty(1 - 2a) \tag{B.11}$$

The theory is applicable when a is between 0 and 0.5 since the velocity has slowed to zero behind the rotor for higher values, which is physically impossible. In fact, the theory breaks down at about $a = 0.35$.

Power is equal to the thrust times the velocity at the disc.

$$P = \frac{1}{2}\rho A_2(U_\infty^2 - U_4^2)U_2 = \frac{1}{2}\rho A_2(U_\infty - U_4)(U_\infty + U_4)U_2 \tag{B.12}$$

substituting equations B.10 and B.11 gives:

$$P = \frac{1}{2}\rho A_2 U_\infty^3 4a(1-a)^2 \tag{B.13}$$

Using equation B.8 gives the power coefficient for the actuator disc:

$$C_p = \frac{P}{\frac{1}{2}\rho U_\infty^3 A_2} = 4a(1-a)^2 \tag{B.14}$$

The power coefficient corresponds to the rotor power divided by the power in the wind. If we put $\frac{dC_p}{da} = 0$, we will get a for maximum C_p.

$$\frac{dC_p}{da} = 4(1-a)^2 - 8a(1-a) = 4(1-4a+3a^2) = 0 \tag{B.15}$$

which gives a maximum C_p when $a = \frac{1}{3}$.

$$C_{p_{max}} = \frac{16}{27} \tag{B.16}$$

The results demonstrate that with the given assumptions, the maximum theoretical power production is $16/27$ of the power in a circular stream-tube with a constant cross section area equal to the disc area. If the free stream velocity is U_∞, then the velocity at the disc is $\frac{2}{3}U_\infty$ and at the end of the stream tube it is $\frac{1}{3}U_\infty$. Therefore, due to continuity, the tube has a cross section area that is $2/3$ of the disc area upstream of the disc and twice the disc area downstream. $C_{p_{max}}$ is generally known as the Betz limit.

The thrust force can be expressed in a similar manner as the power. The non-dimensional thrust coefficient corresponds to the thrust force divided by the dynamic force and can be expressed as:

$$C_T = \frac{T}{\frac{1}{2}\rho U_\infty^2 A_2} \tag{B.17}$$

Combining equations B.6 and B.11 gives:

$$T = \frac{1}{2}\rho A_2 U_\infty^2 \{4a(1-a)\} \tag{B.18}$$

resulting in:

$$C_T = \frac{\frac{1}{2}\rho A_2 U_\infty^2 \{4a(1-a)\}}{\frac{1}{2}\rho A_2 U_\infty^2} = 4a(1-a) \tag{B.19}$$

This page is intentionally left blank.

Appendix C

OpenFOAM

The simulations in this thesis were done using OpenFOAM®, abbreviation of Field Operation And Manipulation, an open source $C++$ based toolbox used for developing customizable numerical solvers to CFD problems. It is free, flexible, and offers a top-level programmable simulation environment where the codes represent the equations directly, e.g.:

The momentum equation:

$$\boxed{\frac{\partial \rho U}{\partial t} + \nabla \cdot \rho U U - \nabla \cdot \mu \nabla U = -\nabla p} \tag{C.1}$$

is coded in OpenFOAM® representation as follows:

```
solve
(
fvm::ddt(rho, U)
+ fvm::div(phi, U)
- fvm::laplacian(mu, U)
==
- fvc::grad(p)
);
```

The pressure used in OpenFOAM® is the kinematic gauge pressure and defines as: $p = (P_abs - P_atm)/\rho$

The codes are released under the GNU General Public License (GPL) that is managed, maintained and distributed by The OpenFOAM® Foundation that is supported by volunteers [88].

C.1 Open source vs Commercial CFD package

The merits of choosing OpenFOAM® over closed source (commercial) software can be summarized as follows:

- Freedom to modify existing or create new solvers.
- Reusibility of pre-compiled functions in the open shared libraries.
- Tailoring capability of compiled solvers for various applications unlike the hard-coded commercial subroutines, leading OpenFOAM® to be more susceptible to research and development applications.

- Consistency through OpenFOAM® distribution since it has all the required applications implying meshing, pre-processing, CFD simulation, post-processing ..etc that are compiled using the built-in functions in its own libraries instead of using external sources.

- Better user involvement in the solution algorithms leading to better related physics understanding.

Furthermore, having the core of OpenFOAM® been programmed by high level C++ adds more merits to the above ones as follows:

- Advanced code debugging at run-time as well as compiling.

- High robustness in its solvers.

- Fast and efficiently managed memory computations.

- Parallel processing capability that possess linear speeds which increase by increasing the processors numbers, hence solving the limited-cores licensing problems in the commercial software [88].

C.2 Chosen solver properties

Table C.1: *pisoFoam* solver properties list in OpenFOAM®

Variables	**Property**	**Value/Type**
p		
	- solver	GAMG
	- tolerance	1e-06
	- relTol	0.1
	- smoother	GaussSeidel
	- nPreSweeps	0
	- nPostSweeps	2
	- cacheAgglomeration	faceAreaPair
	- agglomerator	10
	- mergeLevels	1
pFinal		
	- $p;	
	- tolerance	1e-06
	- relTol	0
(U | k | epsilon | R | nuTilda)		
	- solver	smoothSolver
	- smoother	GaussSeidel
	- tolerance	1e-05
	- relTol	0
PISO algorithm		
	- nCorrectors	2
	- nNonOrthogonalCorrectors	0

C.3 Mesh manipulations

C.3.1 Mesh conversion

It is necessary to convert the mesh from the ANSYS® ICEM CFD format, **.msh**, to OpenFOAM®. The mesh is generated for OpenFOAM® in the "**constant/polyMesh**" folder. To convert the mesh, the **.msh** file should be copied into the current case folder, then by typing the following command:

fluentMeshToFoam **<caseName>**

in the current folder's terminal window, the conversion is completed.

C.3.2 Mesh check

The validity of the mesh should be checked after conversion. Thus, the ***checkMesh*** utility should be run on the newly converted mesh. This will enable the user to take a closer look at cells with problems. The implied geometry tests are bounding box, non-wedge directions, non-empty directions, aspect ratio, cell volumes, mesh non-orthogonality, skewness, and boundary openness.). If the result is "**Mesh OK**", then no problems are found.

C.3.3 Why C-grid?

C-grid is preferred for viscous flow applications since it permits the resolution of the wake, i.e. the grid is aligned to the wake or slipstream at the airfoil trailing edge. The wake and the boundary layer should be adapted in the streamwise direction to be resolved better.

C.4 Numerical analysis schemes

It's worth mentioning that OpenFOAM® is based on finite volume numerical analysis. The numerical schemes involved are summarized in Table C.2.

Table C.2: Numerical schemes list in OpenFOAM®

Schemes Types	**Formula**	**Numerical solution**
ddtSchemes	default	Euler
gradSchemes	default	Gauss linear
divSchemes	default - div(phi,U) - div(phi,k) - div(phi,epsilon) - div(phi,R) - div(R) - div(phi,nuTilda) - div((nuEff*dev(T(grad(U)))))	none - Gauss limitedLinearV 1 - Gauss limitedLinear 1 - Gauss limitedLinear 1 - Gauss limitedLinear 1 - Gauss linear - Gauss limitedLinear 1 - Gauss linear
laplacianSchemes	default	Gauss linear corrected
interpolationSchemes	default	linear
snGradSchemes	default	corrected
fluxRequired	default - p	no

Appendix D

MIRAS-FLEX

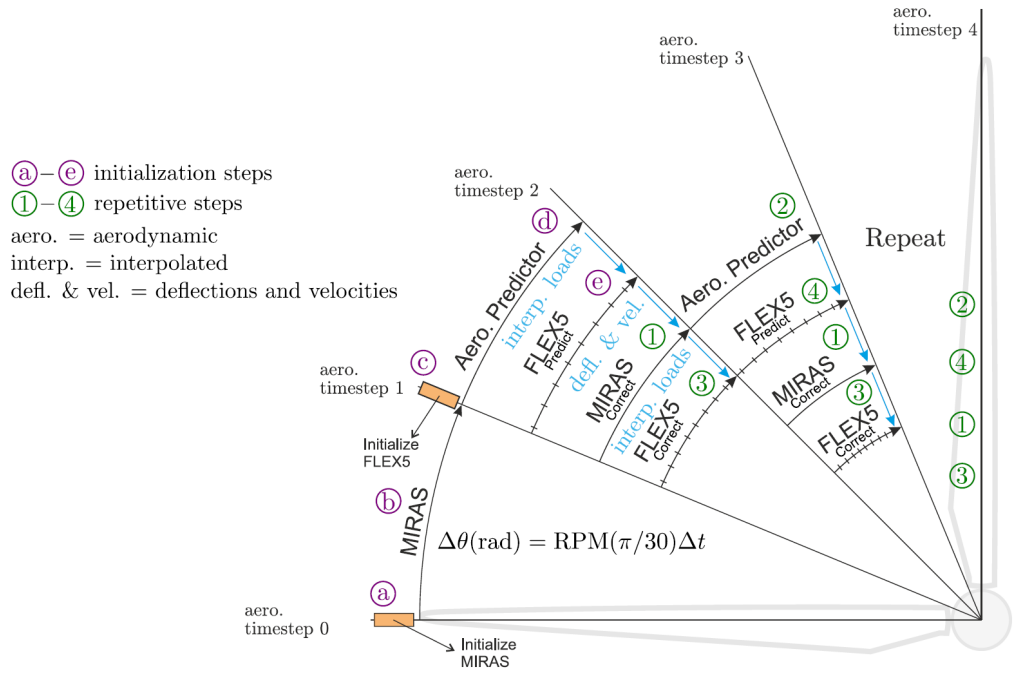

Figure D-1: Azimuthal flow diagram of the predictor–corrector, loosely coupled and multi-rate methodology in MIRAS-FLEX [25].

A predictor–corrector, loosely coupled and multi-rate methodology was chosen to transfer the aerodynamic loads as well as the deformations and velocities between

MIRAS and FLEX5. The methodology is customized to support the explicit time integration schemes in MIRAS and FLEX5. Recall that explicit methods calculate the state of the system at a later time from the state of the system at the current and possibly previous time steps. The methodology is shown in Figure D-1, where MIRAS was selected as the slower subsystem in the multi-rate approach because of its higher computing cost. Loose coupling has been shown to be effective for aeroelastic problems in Heinz et al. [93] and Farhat et al. [94] and the multi-rate approach provides the user the choice to use a more time-efficient solver depending on the simulation. For example, multi-rate will be more efficient for steady cases with few excitations in the aerodynamic forces.

Multi-rate will particularly be useful in optimization studies consisting of steady simulations, and the computational time per call to MIRAS-FLEX must be kept to a minimum. For problems where aerodynamic forces vary in small time steps, one-to-one loose-coupling is performed by setting the time step in MIRAS equal to the smaller time step of FLEX5.

For the case when one-to-one coupling is not used, the smaller time steps of FLEX5 are represented by the tick marks on the FLEX5 arrows in Figure D-1. The instance when MIRAS is called more times than FLEX5 per time step has not been considered in the coupling because of the higher computational cost of MIRAS compared with BEM. Strong coupling was not implemented for the same reason. Even though, the benefits from using strong coupling in place of loose coupling for aeroelastic problems are also not entirely evident. If instabilities occur in simulations, the instabilities might be mitigated by reducing the time step

instead of adding sub-iterations as used in strong coupling [25].

This page is intentionally left blank.

List of Publications

Peer-Reviewed Journal Articles

1. "Numerical Fluid-Structure Interaction Study on the NREL 5MW HAWT.", **Halawa A. M.**, Sessarego M., Shen W. Z. and Yoshida S., Journal of Physics: Conference Series, 1037, 2, pp. 022-026, 2018.

2. "Aerodynamic Performance Enhancement Using Active Flow Control on DU96-W-180 Wind Turbine Airfoil.", **Halawa A. M.**, Elhadidi B., and Yoshida S., Joint Journal of Novel Carbon Resource Sciences and Green Asia Strategy, Evergreen, 5, 1, pp. 16-24, 2018.

3. "System Identification, Fuzzy Control, and Simulation Results For Fixed length Tether of Kite Power System.", Dief T. N., Fechner U., Schmehl R., Yoshida S., Metwally A. M., **Halawa A. M.**, Wind Energy Science, 3, 1, pp. 275-291, 2018.

4. "POD & MLSM Application on DU96-W180 Wind Turbine Airfoil.", **Halawa A. M.**, Elhadidi B., and Yoshida S., Joint Journal of Novel Carbon Resource Sciences and Green Asia Strategy, Evergreen, 4, 1, pp. 36-43, 2017.

Peer-Reviewed Conference Articles

1. "Aerodynamic Performance Validation of DU96-W180 Wind Turbine Airfoil.", **Halawa A. M.**, and Yoshida S., 18^{th} Cross Straits Symposium on Energy and Environmental Science & Technology (CSS-ESST), Shanghai, China, Dec. 4^{th} – 6^{th}, 2016.

2. "Influences of Rotor Thrust on Tower Shadow Effects of Downwind Turbines.", Yoshida S., Takada A., Yoshimizu H., and **Halawa A. M.**, 15^{th} World Wind Energy Conference, Tokyo, Japan, Oct. 31^{st} – Nov. 2^{nd}, 2016.

3. "CFD Analyses of Stall Characteristics of DU96-W180 Wind Turbine Airfoil.", **Halawa A. M.**, and Yoshida S., 15^{th} World Wind Energy Conference, Tokyo, Japan, Oct. 31^{st} – Nov. 2^{nd}, 2016.

4. "Active Flow Control for DU96-W-180 Airfoil at Low Reynolds Number by an "Active Slat"", **Halawa A. M.**, Elhadidi B., and Yoshida S., Asia-Pacific International Symposium on Aerospace Technology (APISAT), Toyama, Japan, Oct. 25^{th} – 27^{th}, 2016.

5. "POD & MLSM Application on DU96-W180 Wind Turbine Airfoil.", **Halawa A. M.**, Elhadidi B., and Yoshida S., 2^{nd} International Exchange and Innovation Conference on Engineering & Sciences (IEICES), Fukuoka, Japan, Oct. 14^{th}, 2016.

6. "Fluid-Structure Interaction Computations for Wind Turbine Blade.", **Halawa A. M.**, and Yoshida S., Grand Renewable Energy (GRE) 2018 International Conference and Exhibition, Yokohama, Japan, June 17^{th} – 22^{nd} , 2018.

7. "Numerical Fluid-Structure Interaction Study on the NREL 5MW HAWT.",

Halawa A. M., Sessarego M., Shen W. Z., and Yoshida S., The Science of Making Torque from Wind (TORQUE) 2018 International Conference, Milan, Italy, June 20^{th} - 22^{nd}, 2018.

This page is intentionally left blank.

Vitae

Amr Halawa was born in Cairo, Egypt in January, 1990. In 2012, he got his Bachelor of Science degree in Aerospace Engineering from the Faculty of Engineering, Cairo University with a 1st rank grade of honor and distinction. Afterwards, he pursed his Master studies in the same department majoring in Aerodynamics and got his Master of Science in Aerospace Engineering in 2015. During the period 2012-2015, he was employed as a teaching assistant in the Aerospace Engineering Department at Cairo University. In October 2015, he joined the Earth System Science and Technology department in the Interdisciplinary Graduate School of Engineering Sciences at Kyushu University as a PhD student working on the numerical modeling and analysis of horizontal axis wind turbines.